Study of B^{0}→ρ^{+}ρ^{-} decays and implications for the CKM angle φ_{2}

P. Vanhoefer *et al.* (Belle Collaboration)

Study of $B^0 \to \rho^+\rho^-$ decays and implications for the CKM angle ϕ_2

P. Vanhoefer,[39] J. Dalseno,[39,63] C. Kiesling,[39] A. Abdesselam,[61] I. Adachi,[16,12] H. Aihara,[68] S. Al Said,[61,31] K. Arinstein,[4,52] D. M. Asner,[54] H. Atmacan,[41] T. Aushev,[43] T. Aziz,[62] V. Babu,[62] I. Badhrees,[61,30] A. M. Bakich,[60] V. Bansal,[54] E. Barberio,[40] P. Behera,[20] B. Bhuyan,[19] J. Biswal,[26] A. Bobrov,[4,52] A. Bozek,[50] M. Bračko,[38,26] T. E. Browder,[15] D. Červenkov,[5] P. Chang,[49] V. Chekelian,[39] A. Chen,[47] B. G. Cheon,[14] K. Chilikin,[42] R. Chistov,[42] V. Chobanova,[39] S.-K. Choi,[13] Y. Choi,[59] D. Cinabro,[74] M. Danilov,[42] N. Dash,[18] J. Dingfelder,[3] Z. Doležal,[5] Z. Drásal,[5] D. Dutta,[62] S. Eidelman,[4,52] H. Farhat,[74] J. E. Fast,[54] T. Ferber,[8] B. G. Fulsom,[54] V. Gaur,[62] N. Gabyshev,[4,52] A. Garmash,[4,52] R. Gillard,[74] Y. M. Goh,[14] P. Goldenzweig,[28] B. Golob,[36,26] D. Greenwald,[64] J. Haba,[16,12] P. Hamer,[11] T. Hara,[16,12] K. Hayasaka,[45] H. Hayashii,[46] X. H. He,[55] T. Horiguchi,[66] W.-S. Hou,[49] T. Iijima,[45,44] K. Inami,[44] A. Ishikawa,[66] R. Itoh,[16,12] Y. Iwasaki,[16] W. W. Jacobs,[21] I. Jaegle,[15] D. Joffe,[29] K. K. Joo,[6] T. Julius,[40] K. H. Kang,[34] E. Kato,[66] P. Katrenko,[43] T. Kawasaki,[51] D. Y. Kim,[58] H. J. Kim,[34] J. B. Kim,[33] J. H. Kim,[32] K. T. Kim,[33] M. J. Kim,[34] S. H. Kim,[14] Y. J. Kim,[32] K. Kinoshita,[7] B. R. Ko,[33] S. Korpar,[38,26] P. Križan,[36,26] P. Krokovny,[4,52] T. Kuhr,[37] T. Kumita,[70] A. Kuzmin,[4,52] Y.-J. Kwon,[76] I. S. Lee,[14] L. Li,[57] Y. Li,[73] L. Li Gioi,[39] J. Libby,[20] D. Liventsev,[73,16] P. Lukin,[4,52] M. Masuda,[67] D. Matvienko,[4,52] K. Miyabayashi,[46] H. Miyata,[51] R. Mizuk,[42,43] G. B. Mohanty,[62] S. Mohanty,[62,72] A. Moll,[39,63] H. K. Moon,[33] T. Mori,[44] E. Nakano,[53] M. Nakao,[16,12] T. Nanut,[26] Z. Natkaniec,[50] M. Nayak,[20] N. K. Nisar,[62] S. Nishida,[16,12] S. Ogawa,[65] S. Okuno,[27] P. Pakhlov,[42] G. Pakhlova,[43] B. Pal,[7] C. W. Park,[59] H. Park,[34] T. K. Pedlar,[77] R. Pestotnik,[26] M. Petrič,[26] L. E. Piilonen,[73] C. Pulvermacher,[28] E. Ribežl,[26] M. Ritter,[39] A. Rostomyan,[8] H. Sahoo,[15] Y. Sakai,[16,12] S. Sandilya,[62] L. Santelj,[16] T. Sanuki,[66] Y. Sato,[44] V. Savinov,[56] O. Schneider,[35] G. Schnell,[1,17] C. Schwanda,[23] A. J. Schwartz,[7] Y. Seino,[51] K. Senyo,[75] O. Seon,[44] M. E. Sevior,[40] V. Shebalin,[4,52] C. P. Shen,[2] T.-A. Shibata,[69] J.-G. Shiu,[49] F. Simon,[39,63] Y.-S. Sohn,[76] A. Sokolov,[24] E. Solovieva,[43] M. Starič,[26] M. Sumihama,[10] T. Sumiyoshi,[70] U. Tamponi,[25,71] Y. Teramoto,[53] K. Trabelsi,[16,12] M. Uchida,[69] T. Uglov,[43] Y. Unno,[14] S. Uno,[16,12] Y. Usov,[4,52] C. Van Hulse,[1] G. Varner,[15] A. Vinokurova,[4,52] A. Vossen,[21] M. N. Wagner,[9] C. H. Wang,[48] M.-Z. Wang,[49] P. Wang,[22] M. Watanabe,[51] Y. Watanabe,[27] E. Won,[33] H. Yamamoto,[66] J. Yamaoka,[54] S. Yashchenko,[8] H. Ye,[8] Y. Yook,[76] Y. Yusa,[51] Z. P. Zhang,[57] V. Zhilich,[4,52] V. Zhulanov,[4,52] and A. Zupanc[26]

(The Belle Collaboration)

[1] University of the Basque Country UPV/EHU, 48080 Bilbao
[2] Beihang University, Beijing 100191
[3] University of Bonn, 53115 Bonn
[4] Budker Institute of Nuclear Physics SB RAS, Novosibirsk 630090
[5] Faculty of Mathematics and Physics, Charles University, 121 16 Prague
[6] Chonnam National University, Kwangju 660-701
[7] University of Cincinnati, Cincinnati, Ohio 45221

[8]*Deutsches Elektronen–Synchrotron, 22607 Hamburg*
[9]*Justus-Liebig-Universität Gießen, 35392 Gießen*
[10]*Gifu University, Gifu 501-1193*
[11]*II. Physikalisches Institut, Georg-August-Universität Göttingen, 37073 Göttingen*
[12]*SOKENDAI (The Graduate University for Advanced Studies), Hayama 240-0193*
[13]*Gyeongsang National University, Chinju 660-701*
[14]*Hanyang University, Seoul 133-791*
[15]*University of Hawaii, Honolulu, Hawaii 96822*
[16]*High Energy Accelerator Research Organization (KEK), Tsukuba 305-0801*
[17]*IKERBASQUE, Basque Foundation for Science, 48013 Bilbao*
[18]*Indian Institute of Technology Bhubaneswar, Satya Nagar 751007*
[19]*Indian Institute of Technology Guwahati, Assam 781039*
[20]*Indian Institute of Technology Madras, Chennai 600036*
[21]*Indiana University, Bloomington, Indiana 47408*
[22]*Institute of High Energy Physics,*
Chinese Academy of Sciences, Beijing 100049
[23]*Institute of High Energy Physics, Vienna 1050*
[24]*Institute for High Energy Physics, Protvino 142281*
[25]*INFN - Sezione di Torino, 10125 Torino*
[26]*J. Stefan Institute, 1000 Ljubljana*
[27]*Kanagawa University, Yokohama 221-8686*
[28]*Institut für Experimentelle Kernphysik,*
Karlsruher Institut für Technologie, 76131 Karlsruhe
[29]*Kennesaw State University, Kennesaw GA 30144*
[30]*King Abdulaziz City for Science and Technology, Riyadh 11442*
[31]*Department of Physics, Faculty of Science,*
King Abdulaziz University, Jeddah 21589
[32]*Korea Institute of Science and Technology Information, Daejeon 305-806*
[33]*Korea University, Seoul 136-713*
[34]*Kyungpook National University, Daegu 702-701*
[35]*École Polytechnique Fédérale de Lausanne (EPFL), Lausanne 1015*
[36]*Faculty of Mathematics and Physics,*
University of Ljubljana, 1000 Ljubljana
[37]*Ludwig Maximilians University, 80539 Munich*
[38]*University of Maribor, 2000 Maribor*
[39]*Max-Planck-Institut für Physik, 80805 München*
[40]*School of Physics, University of Melbourne, Victoria 3010*
[41]*Middle East Technical University, 06531 Ankara*
[42]*Moscow Physical Engineering Institute, Moscow 115409*
[43]*Moscow Institute of Physics and Technology, Moscow Region 141700*
[44]*Graduate School of Science, Nagoya University, Nagoya 464-8602*
[45]*Kobayashi-Maskawa Institute, Nagoya University, Nagoya 464-8602*
[46]*Nara Women's University, Nara 630-8506*
[47]*National Central University, Chung-li 32054*
[48]*National United University, Miao Li 36003*
[49]*Department of Physics, National Taiwan University, Taipei 10617*
[50]*H. Niewodniczanski Institute of Nuclear Physics, Krakow 31-342*

^{51}*Niigata University, Niigata 950-2181*
^{52}*Novosibirsk State University, Novosibirsk 630090*
^{53}*Osaka City University, Osaka 558-8585*
^{54}*Pacific Northwest National Laboratory, Richland, Washington 99352*
^{55}*Peking University, Beijing 100871*
^{56}*University of Pittsburgh, Pittsburgh, Pennsylvania 15260*
^{57}*University of Science and Technology of China, Hefei 230026*
^{58}*Soongsil University, Seoul 156-743*
^{59}*Sungkyunkwan University, Suwon 440-746*
^{60}*School of Physics, University of Sydney, NSW 2006*
^{61}*Department of Physics, Faculty of Science, University of Tabuk, Tabuk 71451*
^{62}*Tata Institute of Fundamental Research, Mumbai 400005*
^{63}*Excellence Cluster Universe, Technische Universität München, 85748 Garching*
^{64}*Department of Physics, Technische Universität München, 85748 Garching*
^{65}*Toho University, Funabashi 274-8510*
^{66}*Tohoku University, Sendai 980-8578*
^{67}*Earthquake Research Institute, University of Tokyo, Tokyo 113-0032*
^{68}*Department of Physics, University of Tokyo, Tokyo 113-0033*
^{69}*Tokyo Institute of Technology, Tokyo 152-8550*
^{70}*Tokyo Metropolitan University, Tokyo 192-0397*
^{71}*University of Torino, 10124 Torino*
^{72}*Utkal University, Bhubaneswar 751004*
^{73}*CNP, Virginia Polytechnic Institute and State University, Blacksburg, Virginia 24061*
^{74}*Wayne State University, Detroit, Michigan 48202*
^{75}*Yamagata University, Yamagata 990-8560*
^{76}*Yonsei University, Seoul 120-749*
^{77}*Luther College, Decorah, Iowa 52101*

Abstract

We present a measurement of the branching fraction and the longitudinal polarization fraction of $B^0 \rightarrow \rho^+ \rho^-$ decays, as well as the time-dependent CP violating parameters in decays into longitudinally polarized $\rho^+ \rho^-$ pairs with Belle's final data set of 772×10^6 $B\bar{B}$ pairs, at the $\Upsilon(4S)$ resonance, collected at the asymmetric-energy $e^+ e^-$ collider KEKB. We obtain

$$\begin{aligned}
\mathcal{B}(B^0 \rightarrow \rho^+ \rho^-) &= (28.3 \pm 1.5 \text{ (stat)} \pm 1.5 \text{ (syst)}) \times 10^{-6}, \\
f_L &= 0.988 \pm 0.012 \text{ (stat)} \pm 0.023 \text{ (syst)}, \\
\mathcal{A}_{CP} &= 0.00 \pm 0.10 \text{ (stat)} \pm 0.06 \text{ (syst)}, \\
\mathcal{S}_{CP} &= -0.13 \pm 0.15 \text{ (stat)} \pm 0.05 \text{ (syst)}.
\end{aligned}$$

We perform an isospin analysis to constrain the CKM angle ϕ_2 and obtain two solutions with

$$\phi_2 = (93.7 \pm 10.6)^\circ,$$

being most compatible with other Standard-Model based fits to the data.

PACS numbers: 11.30.Er, 12.15.Hh, 13.25.Hw

I. INTRODUCTION

CP violation in the Standard Model (SM) is due to an irreducible complex phase in the Cabibbo-Kobayashi-Maskawa (CKM) quark-mixing matrix [1, 2]. Mixing-induced CP violation in the B sector has been clearly observed by the Belle [3, 4] and BaBar [5, 6] collaborations in the $b \to c\bar{c}s$ transition [7] in $B^0 \to J/\psi K_S^0$, while many other modes provide additional information on CP violating parameters [8, 9].

At the $\Upsilon(4S)$ resonance, a quantum-entangled $B^0\bar{B}^0$ pair is produced via $e^+e^- \to \Upsilon(4S) \to B^0\bar{B}^0$. When one of the two B mesons (B_{CP}^0) decays into the CP eigenstate of interest at time t_{CP}, the flavor q of the other B meson (B_{tag}^0, decaying at time t_{tag}) determines the flavor of B_{CP}^0 at the latter time: $q = +1$ for $B_{\text{tag}}^0 = B^0$ and $q = -1$ for $B_{\text{tag}}^0 = \bar{B}^0$. The time interval between the decays of the two B mesons is defined as $\Delta t \equiv t_{CP} - t_{\text{tag}}$ and the time-dependent rate for a B decay into a CP eigenstate is given by

$$\mathcal{P}(\Delta t, q) = \frac{e^{-|\Delta t|/\tau_{B^0}}}{4\tau_{B^0}}\left[1 + q\left(\mathcal{A}_{CP}\cos(\Delta m \Delta t) + \mathcal{S}_{CP}\sin(\Delta m \Delta t)\right)\right]. \tag{1}$$

Here, τ_{B^0} is the B^0 lifetime and Δm the mass difference of the two mass eigenstates of the neutral B meson. $\mathcal{A}_{CP}$ and $\mathcal{S}_{CP}$ are the observables for direct and mixing-induced CP violation, respectively.

In this measurement, we extract the branching fraction $\mathcal{B}$, the fraction of longitudinal polarization of the ρ mesons and the CP-violating parameters in $B^0(\bar{B}^0) \to \rho^+\rho^-$ decays, also referred to as "signal". The CP-violating parameters $\mathcal{A}_{CP}$ and $\mathcal{S}_{CP}$ are measured only for decays into longitudinally polarized ρ mesons. The leading-order tree and penguin diagrams of $B^0 \to \rho^+\rho^-$ decays are shown in Fig. 1. These decays proceed predominantly through the $\bar{b} \to \bar{u}u\bar{d}$ transition and are therefore sensitive to one of the internal angles of the roughly equilateral unitarity triangle, ϕ_2 (or α) $\equiv \arg[(-V_{td}V_{tb}^*)/(V_{ud}V_{ub}^*)]$; its current world average is $(87.7^{+3.5}_{-3.3})°$ [10]. The Belle, BaBar and LHCb collaborations have reported time-dependent CP asymmetries in the following modes: $B^0 \to \pi^+\pi^-$ [11–13], $\rho^\pm\pi^\mp$ [14, 15], $\rho^+\rho^-$ [16–18], $\rho^0\rho^0$ [19, 20] and $a_1^\pm\pi^\mp$ [21–23]. A feature common to these measurements is that possible loop contributions, in addition to the leading-order tree amplitude, can shift the measured angle to $\phi_2^{\text{eff}} \equiv \phi_2 + \Delta\phi_2$, so that the observed mixing-induced CP-violation parameters are related by $\mathcal{S}_{CP} = \sqrt{1 - \mathcal{A}_{CP}^2}\sin(2\phi_2^{\text{eff}})$. This inconvenience can be overcome by estimating $\Delta\phi_2$ using either an isospin analysis [24] or $SU(3)$ flavor symmetry [25].

The $\rho^+\rho^-$ vector-vector state is a superposition of three helicity amplitudes A_0, A_{-1} and A_{+1} with CP-even and -odd contributions. Their fractions can be determined through an
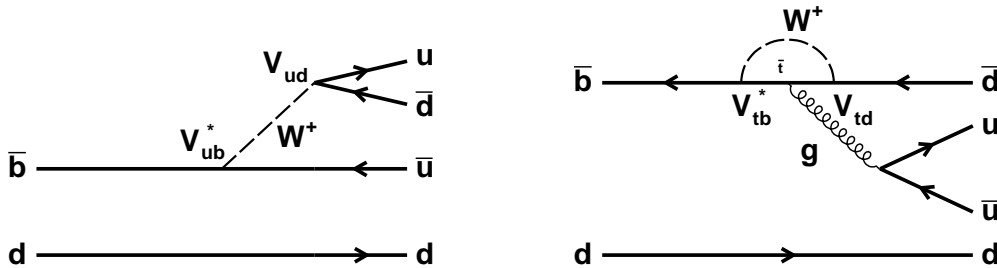

FIG. 1: Leading-order tree (left) and penguin (right) diagrams for the decay $B^0 \to \rho^+\rho^-$.

angular analysis; the $\rho^\pm$ mesons from $B^0 \to \rho^+ \rho^-$ are found to be almost entirely longitudinally polarized [16, 18]. We use the helicity basis, which allows us to separate longitudinally (CP-even, with amplitude A_0) from transversely (CP-even and -odd, with amplitudes $A_\pm$) polarized ρ mesons. The distribution of the two angles θ_H^+ and θ_H^-, each defined as the angle between one of the daughters of the $\rho^\pm$ meson (here, the charged pion) and the B flight direction in the corresponding rest frame of the $\rho^\pm$ (see Fig. 2), is sensitive to the polarization:

$$\frac{1}{\Gamma} \frac{d^2\Gamma}{d\cos\theta_H^+ d\cos\theta_H^-} = \frac{9}{4}\left[\frac{1}{4}(1 - f_L)\sin^2\theta_H^+ \sin^2\theta_H^- + f_L \cos^2\theta_H^+ \cos^2\theta_H^-\right], \qquad (2)$$

where $f_L = |A_0|^2 / \sum |A_i|^2$ is the fraction of longitudinal polarization.

The SM, using perturbative QCD (pQCD) or QCD factorization in the heavy-quark limit [26–33], predicts the $B^0 \to \rho^+ \rho^-$ branching fraction to be $\sim 30 \times 10^{-6}$ and $f_L \sim 1$. Furthermore, no direct CP violation is expected if penguin contributions are found to be small. The previous measurements are summarized in Table I. The main improvements here compared to previous Belle measurements are the increased data sample and the simultaneous extraction of all observables. The inclusion of additional observables in the fit improves the signal-to-background discrimination and allows us to relax selection criteria and consequently increase the signal efficiency.

TABLE I: Previous measurements of $B \to \rho^+ \rho^-$ decays. The first error is statistical and the second is systematic. The Belle results on the branching fraction and f_L (the CP-violating parameters) are obtained from 275×10^6 (384×10^6) $B\bar{B}$ pairs [16, 17]. The BaBar results are obtained from 384×10^6 $B\bar{B}$ pairs [18].

Exp.	$\mathcal{B}[\times 10^{-6}]$	f_L	$\mathcal{A}_{CP}$	$\mathcal{S}_{CP}$
Belle	$22.8 \pm 3.8 \pm 2.6$	$0.94 \pm 0.04 \pm 0.03$	$0.16 \pm 0.21 \pm 0.07$	$0.19 \pm 0.30 \pm 0.07$
BaBar	$25.5 \pm 2.1^{+3.6}_{-3.9}$	$0.992 \pm 0.024^{+0.026}_{-0.013}$	$-0.01 \pm 0.15 \pm 0.06$	$-0.17 \pm 0.20^{+0.05}_{-0.06}$

In Section II, we describe briefly the data set and the Belle detector. The event selection and the model used for the measurement are described in Sections III and IV, respectively.
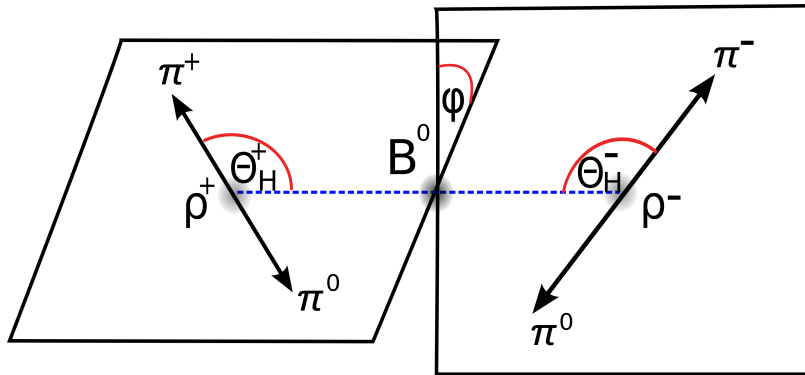

FIG. 2: Definition of the helicity angles $\theta_H^\pm$ for each $\rho^\pm$, identified by its charge.

The results are presented in Section V, followed by validity checks in Section VI. The systematic uncertainties are discussed in Section VII. Constraints on the CKM phase ϕ_2 are presented in Section VIII.

II. DATA SET AND BELLE DETECTOR

This measurement is based on the final data sample containing 772×10^6 $B\bar{B}$ pairs collected with the Belle detector at the KEKB asymmetric-energy e^+e^- (3.5 on 8 GeV) collider [34]. At the $\Upsilon(4S)$ resonance ($\sqrt{s} = 10.58$ GeV), the Lorentz boost of the produced $B\bar{B}$ pairs is $\beta\gamma = 0.425$ along the z direction, which is opposite to the positron beam direction. In addition, 100 fb^{-1} of data about 60 MeV below the $\Upsilon(4S)$ resonance threshold have been recorded and are referred to as "off-resonance" data.

The Belle detector is a large-solid-angle magnetic spectrometer that consists of a silicon vertex detector (SVD), a 50-layer central drift chamber (CDC), an array of aerogel threshold Cherenkov counters (ACC), a barrel-like arrangement of time-of-flight scintillation counters (TOF), and an electromagnetic calorimeter (ECL) comprised of CsI(Tl) crystals located inside a superconducting solenoid coil providing a 1.5 T magnetic field. An iron flux-return yoke located outside of the coil is instrumented to detect K_L^0 mesons and to identify muons. The detector is described in detail elsewhere [35]. Two inner detector configurations were used: a 2.0 cm radius beampipe and a 3-layer silicon strip vertex detector (SVD1) were used for the first sample of 152×10^6 $B\bar{B}$ pairs and a 1.5 cm radius beampipe, a 4-layer silicon strip vertex detector (SVD2) [36] and a small-cell inner drift chamber for the remaining 620×10^6 $B\bar{B}$ pairs. We use a GEANT-based [37] Monte Carlo (MC) simulation to model the response of the detector and to determine its acceptance.

III. EVENT SELECTION

We reconstruct $B^0 \to \rho^+\rho^-$, where $\rho^\pm \to \pi^\pm\pi^0$ and $\pi^0 \to \gamma\gamma$. Charged tracks must satisfy requirements on the distance of closest approach to the interaction point: $|dz| < 5.0$ cm and $dr < 0.5$ cm along and perpendicular to the z axis, respectively. We select charged pions based on particle identification (PID) information from the CDC, ACC and TOF. Our PID requirement on the kaon-pion separation retains 90% of all pions from $B^0 \to \rho^+\rho^-$ decays, but only 10% of all kaons. In addition, we use information from the ECL to veto particles consistent with the electron hypothesis. Requirements of at least two SVD hits in the z projections and one in the azimuthal [38] are imposed on the charged tracks. A π^0 candidate is reconstructed from two photons, identified by isolated energy clusters in the ECL. We suppress combinatorial background by requiring a minimum photon energy of $E_\gamma > 50$ (90) MeV in the ECL barrel (endcap) region and require that the invariant mass of the photon pair to be near the π^0 mass: $|m_{\gamma\gamma} - m_{\pi^0}| < 15$ MeV/c^2, which covers about three times the experimental resolution. We perform a π^0 mass-constraint fit and retain π^0 candidates fulfilling $\chi^2 < 50$ and $p_{\pi^0}^* > 100$ MeV/c, where $p_{\pi^0}^*$ is the momentum of the π^0 in the center-of-mass system (CMS).

Intermediate charged-dipion states are reconstructed within the invariant-mass range 0.4 GeV/c$^2 < m(\pi^\pm\pi^0) < 1.15$ GeV/c^2, covering the broad $\rho^\pm(770)$ resonance [39]. This retains 92% of the phase space available for two $\rho^\pm$ mesons from $B^0 \to \rho^+\rho^-$ decays, while reducing combinatorial background with a tendency for higher dipion masses. Upon com-

bination of two dipion states with opposite charge, a $B^0 \to \rho^+ \rho^-$ candidate is formed. All remaining particles are associated with the accompanying B^0_{tag} meson.

Reconstructed B candidates are described by two kinematic variables: the beam-energy-constrained mass $M_{\text{bc}} \equiv \sqrt{(E^{\text{CMS}}_{\text{beam}}/c^2)^2 - (p^{\text{CMS}}_B/c)^2}$ and the energy difference $\Delta E \equiv E^{\text{CMS}}_B - E^{\text{CMS}}_{\text{beam}}$, where $E^{\text{CMS}}_{\text{beam}}$ is the beam energy and E^{CMS}_B (p^{CMS}_B) is the energy (momentum) of the B meson, evaluated in the CMS. B candidates satisfying $M_{\text{bc}} > 5.27$ GeV/c^2 and $|\Delta E| < 0.15$ GeV are selected for further analysis.

The dominant background contribution arises from continuum events ($e^+e^- \to q\bar{q}$, where $q = u, d, s, c$). We use their jet-like topology to separate them from the more spherical $B\bar{B}$ decays using a Fisher discriminant [40] $\mathcal{F}_{S/B}$, constructed from the following 12 variables (all evaluated in the CMS):

- L^{n}_0, L^{n}_2, L^{c}_2,
  where $L^{\text{k}}_i = \sum_j |\vec{p_j}|(\cos\theta_j)^i$ for neutral clusters (k=n) and charged tracks (k=c) belonging to the tag side, where $i = 0$ or 2, p_j is the momentum of the j-th particle and θ_j the angle between its direction and the thrust axis of the B candidate [18].

- $|\cos(TB, TO)|$,
  cosine of the angle between the thrust axis of the B candidate (TB) and the thrust axis of the remaining tracks (TO).

- $|\cos(TB, z)|$,
  cosine of the angle between TB and the z-axis.

- $\cos(B, z)$,
  the projection of the B flight direction onto the z-axis,

  and the following variables, closely related to the modified Fox-Wolfram moments [41, 42]:

- $h^{c2}_{so}, h^{c4}_{so}, h^{n0}_{so}, h^{n2}_{so}, h^{n4}_{so}, h^2_{oo}$,
  with $h^{km}_{so} = \sum_{i,j} |\vec{p}_{j_k}| P_m(\cos\theta_{ij_k})$, where $\vec{p}_{j_k}$ (here and in the rest of this bullet) is the momentum of the j_k-th particle from the other side (o), the subscript i labels the i-th track from the signal side (s), θ_{ij_k} is the angle between particles i and j_k, and P_m is Legendre polynomial of order m. For o, $k = c$ for charged tracks and $k = n$ for neutral particles, respectively. The quantity $h^2_{oo} = \sum_{i,j} |\vec{p}_i||\vec{p}_j| P_2(\cos\theta_{ij})$ uses only particles from o and does not consider their charge.

The respective distributions and the output are shown in Fig. 3. We require $\mathcal{F}_{S/B} > 0$ to reject 80% of the continuum background while retaining 80% of signal. We use samples with signal MC events and off-resonance data taken below the $\Upsilon(4S)$ resonance for the training of the Fisher discriminant. The requirement on $\mathcal{F}_{S/B}$ together with the previously mentioned requirements of ΔE, M_{bc}, and $m(\pi^\pm\pi^0)$ and the cuts $-0.85 \leq \cos\theta^\pm_{\text{H}} \leq 0.98$ and $|\Delta t| < 70$ ps, define the fit region. The cut of the helicity angles reduces combinatorial background peaking at $\cos\theta^\pm_{\text{H}} \to \pm 1$; the Δt range is also used in independent studies to determine the systematic uncertainties related to the modeling of the Δt distributions.

According to signal MC simulation, 29% of all events have multiple $B^0 \to \rho^+ \rho^-$ candidates. Selecting the B candidate with the smallest sum of the χ^2s from the π^0 mass

constraint fits yields the correct B in 79% of all events with multiple candidates. If both possible dipion combinations of the four pions fall within the fit region, we choose the combination with the larger momentum difference between the daughter pions: longitudinally polarized ρ mesons tend to decay into a high- and low-momentum pion in the CMS frame.

The vertices of the B candidates are determined from their charged tracks [38] and we employ the flavor-tagging method described in Ref. [43]. The tagging information is represented by two parameters: the B^0_{tag} flavor $q = \pm 1$, and the tagging quality r, a continuous, event-by-event flavor tagging dilution factor determined from MC simulation that ranges from zero for no flavor discrimination to unity for unambiguous flavor assignment. We divide the data into seven r-bins, labeled by the index l. The mistagging probability in each r-bin, w, is obtained from studying a high statistics control sample. Thus, the CP asymmetry in data is diluted by a factor $1 - 2w$ instead of the MC-determined r. The performance of the flavor tagging algorithm is then given by $\epsilon_{\text{tag}} = (1 - 2w)^2 \epsilon_{\text{raw}}$, where ϵ_{raw} is the raw tagging efficiency. ϵ_{tag} has been measured to 0.284 ± 0.010 for SVD1 and 0.301 ± 0.004 for SVD2 [4]. We find $\mathcal{F}_{S/B}$ to be correlated with r and provide individual descriptions of $\mathcal{F}_{S/B}$ in each r-bin.

Since the distributions of the fit variables can significantly depend on the number of correctly assigned pions to the reconstructed $\rho^{\pm}$ meson candidates, we consider four categories of reconstruction quality:

a) "truth": all four pions correctly reconstructed,

b) "2T": both charged pions correctly reconstructed and at least one π^0 incorrectly assigned,

c) "1T": only one correctly reconstructed charged pion and no requirement on the π^0 mesons,

d) "0T": anything else.

The total reconstruction efficiencies (percentage of reconstructed events with respect to all generated events) and their decompositions ϵ_i for both polarization states are obtained from MC simulation and are listed in Table II, where, for transverse polarization (TP), the $0T$ fraction is small and so is included in the $1T$ entry. All categories provide useful information for the measurement of the branching fraction and the polarization, while those with at least one correctly reconstructed $\pi^{\pm}$ are used for the time-dependent measurement.

TABLE II: Reconstruction efficiencies (all numbers in percent) for longitudinal (LP) and transverse (TP) polarizations obtained from fully simulated signal MC events.

Mode	truth	$2T$	$1T$	$0T$	Total
$\epsilon_{\text{Sig}}^{\text{SVD1 (LP)}}$ [%]	5.2	1.9	1.3	0.1	8.5
$\epsilon_{\text{Sig}}^{\text{SVD2 (LP)}}$ [%]	6.0	2.2	1.5	0.2	9.9
$\epsilon_{\text{Sig}}^{\text{SVD1 (TP)}}$ [%]	12.0	1.5	0.4	$--$	13.9
$\epsilon_{\text{Sig}}^{\text{SVD2 (TP)}}$ [%]	13.4	1.7	0.4	$--$	15.5

IV. EVENT MODEL

After applying the selection criteria to the data, more than 99% of all events belong to background processes. The branching fraction, ρ polarization fraction and CP-violating parameters of $B^0 \to \rho^+\rho^-$ decays are extracted using an extended unbinned maximum likelihood fit to ΔE, $M_{\rm bc}$, $\mathcal{F}_{S/B}$, M_+, M_-, H_+, H_-, Δt and q in the $l^{\rm th}$ r-bin and SVD configuration s, where $M_\pm$ and $H_\pm$ represent the invariant dipion mass $m(\pi^\pm\pi^0)$ and helicity parameter $\cos\theta_{\rm H}^\pm$ of the $\rho^\pm$ candidate with corresponding charge, respectively. Besides signal, we consider continuum, four different combinatorial backgrounds from other B decays (neutral and charged B decays into charm and charmless final states) and seven B decay modes with a $\pi^+\pi^0\pi^-\pi^0$ final state: $B^0 \to a_1^\pm\pi^\mp$, $a_1^0\pi^0$, $\omega\pi^0$, and the non-resonant final states $(\rho^\pm\pi^\mp\pi^0)_{\rm NR}$, $(\rho^0\pi^0\pi^0)_{\rm NR}$, $(f_0(980)\pi^0\pi^0)_{\rm NR}$, and $(\pi^+\pi^0\pi^-\pi^0)_{\rm NR}$. These four-pion final states are referred to as peaking backgrounds since their ΔE and $M_{\rm bc}$ distributions mimic the signal. For the signal and background components, probability density functions (PDFs) are defined with parameters adjusted to describe the MC distributions for each of the nine observables in the l, s data subsamples. The PDF for event i is given by $\mathcal{P}(\Delta E^i, M_{\rm bc}^i, \mathcal{F}_{S/B}^i, M_+^i, M_-^i, H_+^i, H_-^i, \Delta t^i, q^i)$. Correlations between or among observables are taken into account by incorporating a dependence of one variable's PDFs parameters on the correlated variable(s). The component's PDF is taken as the product of individual PDFs for each fit variable $\mathcal{P}(j)$. A summary of the model including all correlations that are accounted for is given in Table III and a detailed and complete description of the model is provided in Ref. [44].

In analogy to the signal model, we consider up to three different reconstruction categories for background processes where $\rho^\pm$ resonances can be reconstructed: both ($2T$), one ($1T$), or no charged pion ($0T$) originating from the $\rho^\pm$ resonance. In the case of only one correct track ($1T$), the distributions of the dipion masses and helicity angles depend strongly on the charge of the correctly reconstructed track (see e.g. Eq.IV A 3). We account for this in the description of the likelihood by considering each case (ρ^+ or ρ^-) separately, but symmetrizing the PDFs such that the PDFs with a correct ρ^+ are identical to those with a correct ρ^- when interchanging the label ($+ \leftrightarrow -$). All relevant components are found to be charge symmetric and have equal fractions of positively and negatively charged $\rho^\pm$ mesons.

The dipion resonances are described by a relativistic Breit-Wigner (BW)

$$BW(m_{\pi\pi}) \equiv \frac{m_0\Gamma(m_{\pi\pi})}{(m_{\pi\pi}^2 - m_0^2)^2 + m_0^2\Gamma^2(m_{\pi\pi})}, \tag{3}$$

with a mass-dependent width

$$\Gamma(m_{\pi\pi}) = \Gamma_0\left(\frac{p_\pi}{p_0}\right)^3\left(\frac{m_0}{m_{\pi\pi}}\right)B_1^2(p_\pi), \tag{4}$$

where p_π is the momentum of either resonance daughter in the resonance frame and $m_{\pi\pi}$ is the invariant mass of the dipion pair. Γ_0 and m_0 are the width and mass of the nominal resonance and p_0 is the nominal momentum of either pion daughter from a nominal ρ. $B_1(p_\pi) = \sqrt{\frac{1+(3p_0)^2}{1+(3p_\pi)^2}}$ is the Blatt-Weisskopf form factor, as described in Ref. [45]. The PDFs for $\mathcal{F}_{S/B}$ for all components (signal) are sums of two (three) bifurcated Gaussian functions in each r-bin.

TABLE III: Summary of the parametrization for each component in the fit model. The details are provided in Ref. [44]. Up to three different reconstruction categories are considered for entries with superscript $nT \in 2T$, $1T$, $0T$ (see text). The variables in the subscript list the identifed correlations. The PDFs for the dipion-masses and helicity angles are usually correlated; here we only show a one-dimensional simplification. C stands for sums of Chebyshev polynomials, H for histograms, A for an ARGUS function, (t/db)G for a (triple/double-bifurcated) Gaussian function (the subscript l indicating separate descriptions in each r-bin), BW for a relativistic Breit-Wigner function and $\exp_\mathcal{R}$ for an exponential function convoluted with a resolution function ($\mathcal{R}$), where the superscript CP labels an included CP asymmetry term depending on the flavor q of $B_{\rm tag}^0$. For the signal Δt PDFs, $|_{\rm eff.}^{\rm truth}$ implies shared CP violation parameters with the respective truth model for longitudinal or transverse polarization, respectively, using an effective lifetime (see text).

Mode	ΔE	$M_{\rm bc}$	$m(\pi^\pm\pi^0)$	$\cos\theta_{\rm H}^\pm$	$\mathcal{F}_{S/B}$	Δt
Truth (LP)	(dbG+C)	$\text{dbG}|_{\Delta E}$	$\text{BW}|_{\Delta E}$	Eq. (2)$|_{\Delta E}$	tbG_l	$\exp_\mathcal{R}^{CP}$
2T (LP)	$(\text{dbG+C})|_{\cos\theta_{\rm H}}$	$(\text{dbG+A})|_{\Delta E \cos\theta_{\rm H}}$	$(\text{BW+C})|_{\cos\theta_{\rm H}}$	H	$\text{dbG}_l^{\rm sig}|_{\Delta E}$	truth (LP)
1T (LP)	$(\text{dbG+C})|_{\cos\theta_{\rm H}}$	(dbG+A)	$(\text{BW+C})^{1T}$	H^{1T}	$\text{dbG}_l^{\rm sig}$	$\exp_\mathcal{R}^{CP}|_{\rm eff.}^{\rm truth}$
0T (LP)	dbG+C	dbG+A	BW+C	H	$\text{dbG}_l^{\rm sig}$	$\exp_\mathcal{R}$
Truth (TP)	(dbG+C)	dbG	$\text{BW}|_{\Delta E}$	Eq. (2)	$\text{dbG}_l^{\rm sig}$	$\exp_\mathcal{R}^{CP}$
2T (TP)	$(\text{dbG+C})|_{\cos\theta_{\rm H}}$	dbG+A	H	H	$\text{dbG}_l^{\rm sig}$	truth (TP)
1T (TP)	C	dbG+A	H	H	$\text{dbG}_l^{\rm sig}$	$\exp_\mathcal{R}^{CP}|_{\rm eff.}^{\rm truth}$
$a_1^\pm\pi^\mp$	dbG+C	dbG+A	$(\text{BW+C})^{nT}$	H^{nT}	$\text{dbG}_l^{\rm sig}$	$\exp_\mathcal{R}^{CP}$
$a_1^0[\rho^\pm\pi^\mp]\pi^0$	dbG+C	dbG+A	H^{nT}	H^{nT}	$\text{dbG}_l^{\rm sig}$	$\exp_\mathcal{R}^{CP}$
$a_1^0[\rho^0\pi^0]\pi^0$	dbG+C	dbG+A	$\text{C}|_{\cos\theta_{\rm H}}$	G+C	$\text{dbG}_l^{\rm sig}$	$\exp_\mathcal{R}^{CP}$
$\omega\pi^0$	dbG+C	dbG+A	$(\text{G+C})|_{\cos\theta_{\rm H}}$	(G+C)	$\text{dbG}_l^{\rm sig}$	$\exp_\mathcal{R}^{CP}$
$(4\pi)_{\rm NR}$	dbG+C	dbG+A	C	C	$\text{dbG}_l^{\rm sig}$	$\exp_\mathcal{R}^{CP}$
$(\rho^\pm\pi^\mp\pi^0)_{\rm NR}$	$(\text{dbG+C})^{nT}|_{M_{\rm bc},\cos\theta_{\rm H}}$	$(\text{dbG+A})_{\cos\theta_{\rm H}}$	$(\text{BW+C})^{nT}|_{\cos\theta_{\rm H}}$	H^{nT}	$\text{dbG}_l^{\rm sig}$	$\exp_\mathcal{R}^{CP}$
$(\rho^0\pi^0\pi^0)_{\rm NR}$	dbG+C	dbG+A	C	H	$\text{dbG}_l^{\rm sig}$	$\exp_\mathcal{R}^{CP}$
$(f_0\pi^0\pi^0)_{\rm NR}$	dbG+C	dbG+A	C	H	$\text{dbG}_l^{\rm sig}$	$\exp_\mathcal{R}^{CP}$
continuum	$\text{C}^{nT}|_{\mathcal{F}_{S/B}}$	A	$(\text{BW+C})^{nT}$	$\text{C}^{nT}|_{m(\pi^\pm\pi^0)}$	dbG_l	$\exp_\mathcal{R}$
$B_{\rm charm}^0$	C^{nT}	A	$(\text{BW+C})^{nT}|_{\cos\theta_{\rm H}}$	C^{nT}	$\text{dbG}_l^{\rm sig}$	$\exp_\mathcal{R}$
$B_{\rm charm}^+$	C^{nT}	A	$(\text{BW+C})^{nT}|_{\cos\theta_{\rm H}}$	C^{nT}	$\text{dbG}_l^{\rm sig}$	$\exp_\mathcal{R}$
$B_{\rm charmless}^0$	$\text{C}^{nT}|_{\cos\theta_{\rm H}}$	$(\text{dbG+A})|_{\Delta E}$	$(\text{BW+C})^{nT}|_{\cos\theta_{\rm H},\Delta E}$	$\text{C}^{nT}|_{\Delta E}$	$\text{dbG}_l^{\rm sig}$	$\exp_\mathcal{R}$
$B_{\rm charmless}^+$	$\text{C}^{nT}|_{\cos\theta_{\rm H}}$	A	$(\text{BW+C})^{nT}|_{\cos\theta_{\rm H}}$	C^{nT}	$\text{dbG}_l^{\rm sig}$	$\exp_\mathcal{R}$

A. Signal Model

The $B^0 \to \rho^+\rho^-$ model consists of seven parts (see Tables II and III) and is determined from fully simulated signal MC events for each ρ polarization state (LP and TP) and each reconstruction category. For each polarization, the CP violation parameters are made common among the Truth, 2T and 1T (but not 0T) components. The correlation matrices for all signal components with longitudinal polarization are given in Section IX.

1. Truth Model

For both polarizations, the truths model's ΔE distributions are described by the sum of two bifurcated Gaussians (dbG) and a straight line. The $M_{\rm bc}$ PDFs are taken to be dbGs, where for longitudinal polarization, the mean and width of the core Gaussian of $M_{\rm bc}$ depend on ΔE. $\mathcal{F}_{S/B}$ is modeled as described above, for transverse polarization, the second and third Gaussians of the $\mathcal{F}_{S/B}$ PDFs are taken from longitudinal polarization.

The $\rho^\pm$ mass is modeled with a BW, whose mean and the width depend slightly on ΔE. In the fit to data the nominal mean and width of the BW are fixed to the values given in Ref. [39]. The PDFs are weighted with a mass-dependent reconstruction efficiency, being obtained from fully simulated MC events for each polarization.

We use the corresponding part of Eq. 2 to describe the helicity distribution of each polarization. The PDFs are weighted with binned, two-dimensional, symmetrized ($\cos\theta_{\rm H}^+ \leftrightarrow \cos\theta_{\rm H}^-$), helicity-angle dependent reconstruction efficiencies obtained from fully simulated signal MC events. For longitudinal polarization we account for the correlation of the helicity angles with ΔE by using separate reconstruction efficiency histograms in five bins of ΔE.

Each polarizations PDF for Δt is taken to be

$$
\mathcal{P}_{{\rm truth},l,s}^{\rm LP(TP)}(\Delta t, q) \equiv \frac{e^{-|\Delta t|/\tau_{B^0}}}{4\tau_{B^0}} \Big\{ 1 - q\Delta w^{l,s} + q(1 - 2w^{l,s}) \times
$$
$$
\Big[\mathcal{A}_{CP}^{\rm LP(TP)} \cos(\Delta m \Delta t) + \mathcal{S}_{CP}^{\rm LP(TP)} \sin(\Delta m \Delta t) \Big] \Big\} \otimes \mathcal{R}_{B^0\bar{B}^0}^s(\Delta t). \tag{5}
$$

where $w^{l,s}$ accounts for the CP dilution due to the probability of tagging the wrong $B_{\rm tag}^0$ flavor q and $\Delta w^{l,s}$ accounts for the wrong tag difference between B and $\bar{B}$. Both are determined from flavor specific control samples. The B^0 lifetime, τ_{B^0}, and the mass difference between the two mass eigenstates B_H^0 and B_L^0, Δm, are taken from Ref. [39]. The Δt PDF is convolved with the resolution function described in [38].

2. Two Tracks (2T) Model

The ΔE distribution is modeled with the sum of a dbG and a straight line, where the mean of the core Gaussian, the fraction of the line and its slope depend on the helicity angles. $M_{\rm bc}$ is described by the sum of a dbG and an Argus function. For LP, their relative fraction depends on ΔE and the helicity angles. The $\mathcal{F}_{S/B}$ distributions are described similar to the ones used for the transverse polarized truth model. In addition, for longitudinal polarization the widths of each core Gaussians of $\mathcal{F}_{S/B}$ depend on ΔE. A wrongly assigned π^0 is broaden up the resonance peak in the mass distribution and is also shifting the helicity angles towards negative values. The mass PDF is the product of the sum of a second order

11

Chebychev polynomial and a BW for each mass, where the relative fractions as well as the width of one of the BWs depends on the helicity angles. A two-dimensional histogram is taken for transverse polarization. The $\cos\theta_{\mathrm{H}}^+$-$\cos\theta_{\mathrm{H}}^-$ PDFs for each polarization are taken to be two-dimensional histograms. Since only charged tracks contribute to the determination of Δt, its PDF is identical to the one used in the truth model (see Eq. (5)).

3. One Track (1T) Model

The ΔE distribution is modeled with the sum of a dbG and a straight line for longitudinal polarization, where the relative fraction and the slope depend on the helicity angles. The ΔE distribution for transverse polarization is described by a straight line. M_{bc} is described by the sum of a dbG and an Argus function. The distributions of the dipion masses and helicity angles depend on the charge of the correctly reconstructed $\pi^{\pm}$. For longitudinal polarization, the $m_{\pi^{\pm}\pi^0}$ distribution including the correctly reconstructed $\pi^{\pm}$ is described by the sum of a BW and a second order Chebychev polynomial, $\mathcal{P}^{\mathrm{OK}}(m(\pi^{\pm}\pi^0))$, while the $m_{\pi^{\pm}\pi^0}$ distribution with the fake track from B_{tag} is modeled by the sum of Chebychev polynomials up to the fifth order, $\mathcal{P}^{\mathrm{fake}}(m(\pi^{\pm}\pi^0))$. The helicity PDFs are taken to be two-dimensional histograms, $\mathcal{P}^{\pm}(\cos\theta_{\mathrm{H}}^+, \cos\theta_{\mathrm{H}}^-)$, where we distinguish the two cases of the charge of the correctly reconstructed $\rho^{\pm}$. The PDF of the $m_{\pi^+\pi^0}$-$m_{\pi^-\pi^0}$-$\cos\theta_{\mathrm{H}}^+$-$\cos\theta_{\mathrm{H}}^-$ distribution is then given by

$$\mathcal{P}_{1\mathrm{T}}^{\mathrm{LP}}(m_{\pi^+\pi^0}, m_{\pi^-\pi^0}, \cos\theta_{\mathrm{H}}^+, \cos\theta_{\mathrm{H}}^-) \equiv$$
$$f_+ \mathcal{P}^{\mathrm{OK}}(m_{\pi^+\pi^0})\mathcal{P}^{\mathrm{fake}}(m_{\pi^-\pi^0})\mathcal{P}^+(\cos\theta_{\mathrm{H}}^+, \cos\theta_{\mathrm{H}}^-) +$$
$$(1 - f_+)\mathcal{P}^{\mathrm{fake}}(m_{\pi^+\pi^0})\mathcal{P}^{\mathrm{OK}}(m_{\pi^-\pi^0})\mathcal{P}^-(\cos\theta_{\mathrm{H}}^+, \cos\theta_{\mathrm{H}}^-)$$

where the fraction of events with a correctly reconstructed π^+, f_+ is made common among the detector configurations SVD1 and SVD2. We ignore such a correlation for transverse polarization, since f_L has been measured to be close to one [16–18]. The ρ masses and helicity angle distributions for transverse polarization are each modeled with two-dimensional histograms.

The PDF for $\mathcal{F}_{S/B}$ is similar to the one used for the transverse polarized truth model. Even with only one correctly reconstructed track it is possible to use the Δt distribution to obtain CP violation related information. The Δt PDF is described by Eq. (5) with an effective lifetime that accounts for the contamination from the wrongly assigned track.

4. Zero Track (0T) Model

Because the transverse polarization's fraction without any correctly reconstructed tracks is negligible, we include those events in the model used for transverse polarization when one $\pi^{\pm}$ is correctly reconstructed. For longitudinal polarization, the ΔE distribution is modeled with the sum of a dbG and a first order Chebychev polynomial and the M_{bc} distribution is described by the sum of a dbG and an Argus function. Each $m_{\pi^{\pm}\pi^0}$ distribution is modeled with the sum of a BW, a second and a third order Chebychev polynomial and the PDF for the $\cos\theta_{\mathrm{H}}^+$-$\cos\theta_{\mathrm{H}}^-$ distribution is taken to be a histogram. The Δt PDFs for the "0T" components are parameterized as

$$\mathcal{P}_{0\mathrm{T}}^{\mathrm{LP(TP)}}(\Delta t) \equiv \frac{1}{2\tau_{0\mathrm{T}}}e^{-|\Delta t|/\tau_{0\mathrm{T}}} \otimes \mathcal{R}_{0\mathrm{T}}(\Delta t), \tag{6}$$

with an effective lifetime τ_{0T} and convoluted with the sum of two Gaussian functions $(G(x, \mu, \sigma))$ with a common mean μ

$$\mathcal{R}_{0T}(\Delta t) \equiv (1 - f_{\text{tail}})G(\Delta t, \mu, S_{\text{core}}\sigma) + f_{\text{tail}}G(\Delta t, \mu, S_{\text{core}}S_{\text{tail}}\sigma). \tag{7}$$

The second Gaussian function accounts for a broader tail and its width is related to that of the core Gaussian $S_{\text{core}}\sigma$ through a multiplicative factor S_{tail}. The scale factor $S_{\text{core}} \equiv \sqrt{\sigma_{\text{Rec}}^2 + \sigma_{\text{tag}}^2}/\beta\gamma c$ is an event-dependent error on Δt constructed from the vertex resolution of B_{CP}^0 (σ_{Rec}) and B_{tag}^0 (σ_{tag}). We use a different set of Gaussian functions if at least one of the B vertices is obtained from only one track.

B. Continuum Model

The continuum model consists of three components ($2T$, $1T$ and $0T$) and is studied with continuum MC simulation. To reduce the systematic uncertainty related to a fixed parametrization, some parameters of the continuum model are floated in the fit to data; the initial values for these model parameters are obtained from the fits to MC simulation. The PDF description is confirmed with on-resonance (almost entirely continuum events, after reconstruction) and off-resonance data. The correlations between the helicity angles and the dipion masses are taken into account and this description is confirmed by projecting into several slices of one of the variables and comparing the projected shapes of the other distribution in the two data sets.

The ΔE distributions of all continuum components are described by the sum of a first and a second order Chebychev polynomial, where the first order one depends on $\mathcal{F}_{S/B}$. The dependence slightly differs for the three different reconstruction categories. The M_{bc} distributions of all reconstruction types is commonly described by an Argus function. Because we find a small difference in the r-bin distributions of the $\pm, 0$ and $2c\pi$ components, we use different r-bin fractions for each of the three categories.

For the description of the mass and helicity angle distributions we use certain combination of two kinds of one-dimensional PDFs; one for distributions including a $\rho^\pm$ resonance and one otherwise. The different reconstruction types are then described by combinations of these PDFs. This reduces the degrees of freedom in the fit to data, where the parameters of the continuum model are floated. The mass PDF for the distributions including a $\rho^\pm$ resonance is given by a sum of a BW and Chebychev polynomials. The sum of a bifurcated Gaussian and Chebychev polynomials is describing the combinatorial background. The helicity PDFs for for distributions for both cases, including a $\rho^\pm$ resonance and otherwise, are given by the sums of Chebychev polynomials up to the ninth order. Due to a correlation with the dipion masses, some of the helicity parameters depend on the dipion masses.

The Δt PDF is the sum of Eq. (6) and a delta function. The latter accounts for the prompt production of light quarks (u, d, s) in addition to the exponential decay that describes the production of charm quarks with an effective lifetime $\tau_{q\bar{q}}$:

$$\mathcal{P}_{q\bar{q}}(\Delta t) \equiv \left[(1 - f_\delta)\frac{e^{-|\Delta t|/\tau_{q\bar{q}}}}{2\tau_{q\bar{q}}} + f_\delta \delta(\Delta t - \mu_{q\bar{q}})\right] \otimes \mathcal{R}_{q\bar{q}}(\Delta t). \tag{8}$$

The resolution function $\mathcal{R}_{q\bar{q}}$ is similar to Eq. (7).

C. $B\bar{B}$ **Model**

The model for combinatorial background from other B decays is obtained from four separate sets of MC simulation: neutral and charged B meson decays into charmed and charmless final states. The samples contain 10 and 50 times the number of expected charmed and charmless events in the data, respectively. In the case of neutral B meson decays into charmless final states, the four-pion modes are excluded from the MC sample as they are treated separately (see Section IV D). In the fit model, we further distinguish the reconstruction categories $2T$, $1T$ and $0T$; the $2T$ category is only a significant contribution for charged B decays. The fraction of events for each charged B model is fixed relative to the number of the corresponding neutral model as obtained from MC simulation and is given in Table IV (the distributions for charm final states being almost identical). The Δt PDFs are similar to Eq. (6), with an effective lifetime for each component.

1. *Charm* $\boldsymbol{B^0}$ *Backgrounds*

The ΔE distributions for all three reconstruction categories of charm B^0 decays are described by the sum of Chebychev polynomials up to the second order, and the $M_{\rm bc}$ distributions are described by Argus functions. The PDF of the $m(\pi^{\pm}\pi^0)$ distributions including one correctly reconstructed $\rho^{\pm}$ meson is given by the sum of a BW, a second and a third order Chebychev polynomial, where the fraction of the BW depends on the helicity angles. The distributions without a correctly reconstructed $\rho^{\pm}$ meson are take to be sums of Chebychev polynomial up to the fifth order. The distributions of the helicity angles are modeled by the products of sums of Chebychev polynomials up to the eighth order for each reconstruction category.

2. *Charm* $\boldsymbol{B^{\pm}}$ *Backgrounds*

The PDFs of the ΔE, $M_{\rm bc}$, $m_{\pi^{\pm}\pi^0}$ and helicity distributions are similarly described as those of neutral B decays into charm final states. For the mass PDF, a correlation with the helicity angles is included for the component including a correctly reconstructed $\rho^{\pm}$ meson. For the 2T component, the mass and helicity distributions are taken to be the sum of a BW and a second order Chebychev polynomial and the sums of Chebychev polynomials up to the eighth order, respectively.

3. *Charmless* $\boldsymbol{B^0}$ *Backgrounds*

The ΔE distributions are described by sums of Chebychev polynomials up to the forth order, where a correlation with the helicity angles is accounted for in the case of a correctly reconstructed $\rho^{\pm}$ meson. The $M_{\rm bc}$ distributions are described by Argus functions. In the case of a correctly reconstructed $rho^{\pm}$ resonance, a dbG is added. Its relative fraction depends on ΔE and the helicity angles.

The PDF of the $m_{\pi^+\pi^0}$-$m_{\pi^-\pi^0}$ distribution of the 1T component is given by the the product of a BW added to the sum of Chebychev polynomials up to the third order for each dipion mass, where the fraction of the BW of the correctly reconstructed resonance depends

on the helicity angles. The product of a sum of Chebychev polynomial up to the fifth order is taken if no $\rho^\pm$ resonance has been correctly reconstructed. The distribution of the helicity angles is modeled by the product of sums of Chebychev polynomials up to the eighth order for each reconstruction category. A correlation with ΔE is accounted for in the case of a correctly reconstructed $\rho^\pm$ resonance.

4.   Charmless $B^\pm$ Backgrounds

The ΔE distributions are described by sums of Chebychev polynomials up to the third order. A correlation with the helicity angles is included for the reconstruction category 1T. The PDF for M_{bc} is an Argus function. The mass distributions are described by the sum of a BW and Chebychev polynomials in the case of a correctly reconstructed $\rho^\pm$ resonance and by sums of Chebychev polynomials otherwise. A correlation of the $\rho^\pm$ masses with the helicity angles is included in the description of all reconstruction categories. The PDFs for the helicity angles are taken to be sums of Chebychev polynomials.

D.   Peaking Background Model

The PDFs of the remaining four-pion states are determined from individually generated MC samples. We consider the following final states from B^0 decays (the subscript NR denoting a non-resonant multi-meson state): $(\pi^+\pi^0\pi^-\pi^0)_{\mathrm{NR}}$, $a_1^\pm[\rho^\pm\pi^0]\pi^\mp$, $a_1^0\pi^0$, $(\rho^\pm\pi^\mp\pi^0)_{\mathrm{NR}}$, $(\rho^0\pi^0\pi^0)_{\mathrm{NR}}$, $(f_0(980)[\pi^+\pi^-]\pi^0\pi^0)_{\mathrm{NR}}$ and $\omega[\pi^+\pi^-\pi^0]\pi^0$. The numbers of expected $B \to a_1^\pm\pi^\mp$ and $B \to \omega\pi^0$ events are fixed according to their world average branching fractions [39]; the other four-pion modes are poorly known and their yields are allowed to float in the fit.

Since only one dipion combination from $B \to \omega[\pi^+\pi^-\pi^0]\pi^0$ lies in the signal window, this non-peaking mode has a very small reconstruction efficiency: only one event is expected and the model is described in Ref. [44].

If no other description is explicitly mentioned, we use a dbG to model the ΔE distributions of all peaking backgrounds. The tail Gaussian is obtained from correctly reconstructed $B^0 \to \rho^+\rho^-$ MC events and is made common among all four-pion final states. The sum of Chebychev polynomials up to the third order is added in order to describe underlying combinatorial background from wrongly assigned tracks. The M_{bc} distributions of the four-pion final states are described by a dbG for correctly reconstructed tracks plus an Argus function for the combinatorial background. The $\mathcal{F}_{S/B}$ distribution of all four-pion states are described similarly to the one used for the transverse polarized truth model and each Δt PDF is similar to Eq. (5).

1.   Model For $B^0 \to (\pi^+\pi^0\pi^-\pi^0)_{\mathrm{NR}}$ Decays

The distribution of each mass is modeled by the sum of a second and a third order Chebychev polynomial and the distribution of each helicity angle is described by the sum of Chebychev polynomials up to the eighth order.

2.   Model For $B^0 \to a_1\pi$ Decays

We consider both decays $B^0 \to a_1^\pm \pi^\mp$ and $B^0 \to a_1^0 \pi^0$ separately, where the latter decay is further separated into two different possible decays of the a_1^0: $a_1^0 \to \rho^\pm \pi^\mp$ and $a_1^0 \to \rho^0 \pi^0$.

- Model for $B^0 \to a_1^\pm \pi^\mp$ Decays

We consider only the subsequent decay $a_1^\pm \to \rho^\pm \pi^0$ as the decay $B^0 \to a_1^\pm[\rho^0\pi^\pm]\pi^\mp$ yields in a different final state and is included in the non-peaking B^0 decays into charmless final states. We assume isospin symmetry and set the fraction of $a_1^\pm$ decaying to $\rho^\pm\pi^0$ to be 50%. Because of the high momentum of the $\pi^\mp$, the helicity angle associated with a $\pi^\pm\pi^0$ pair reconstructed with the $\pi^\mp$ from the B decay peaks sharply at $\cos\theta_H = -1$. Therefore, the helicity angles are especially useful in separating this component from others. We consider a 1T and a 0T contribution in the description of the mass and helicity PDFs. The mass PDF for the 1T part is the sum of a BW and a second order Chebychev polynomial for the correctly reconstructed $\rho^\pm$ meson multiplied with the sum of Chebychev polynomials. The mass distribution without a correctly reconstructed ρ resonance is described by the sum of Chebychev polynomials up to the fifth order for each mass. The helicity PDFs for all cases of reconstruction are histograms from fully simulated MC events.

- Model For $B^0 \to a_1^0 \pi^0$ Decays

Three dominant subsequent decays of the $a_1^0 \to \rho\pi$ yield in the same final state as our signal, $a_1^0 \to \rho^+\pi^-, \rho^-\pi^+, \rho^0\pi^0$. We assume that their amplitudes are of similar size, because of isospin arguments. A common PDF is used to describe the Δt distribution.

- $B^0 \to a_1^0[\rho^\pm\pi^\mp]\pi^0$

We have a common model for $a_1^0 \to \rho^\pm\pi^\mp$ decays, where we furthermore distinguish between the different reconstruction categories 1T and 0T, due to misreconstruction. Opposite to $B^0 \to a_1^\pm\pi^\mp$ decays, the fast pion is neutral, therefore the corresponding helicity distributions peak at $\cos\theta_H = +1$. The mass and helicity PDFs for all reconstruction categories are individual two-dimensional histograms. We use a PDF similar to Eq. (6) with an effective lifetime to account for the contamination from wrong side tracks for the reconstruction category 0T.

- Model For $B^0 \to a_1^0[\rho^0\pi^0]\pi^0$ Decays

This decay does not contain a $\rho^\pm$ resonance, hence no separate treatment is needed. The mass PDF is the product of distinct sums of Chebychev polynomials up to the fifth order, whose combinations depend on the helicity angles (if $\cos\theta_H^+ > \cos\theta_H^-$ or else). The PDF for the helicity angles is the product of sums of two Gaussians and a second order Chebychev polynomial

3.   Model For $B^0 \to (\rho^\pm\pi^\mp\pi^0)_{\mathrm{NR}}$ Decays

Since there is no suitable decay model for a pseudo-scalar decaying into a vector particle and two pseudo-scalars, we assume a phase-space model and account for that assumption in the systematic uncertainty. We consider the categories 1T and 0T separately. For the cate-

gory 1T a correlation of ΔE with M_{bc} and the helicity angles is accounted for by introducing a dependence of the relative fraction of the dbG of the ΔE PDF. The ΔE distribution for reconstruction category 0T is described by a first order Chebychev polynomial. The relative fraction of the dbG of the M_{bc} PDF for events of category $1T$ depends on the helicity angles. The mass distributions for both reconstruction categories are described similar to the $B^0 \to a_1^{\pm}\pi^{\mp}$ model, in addition, the fraction of the resonant part depends on the helicity angles for the category $1T$. The PDF for the helicity distribution is taken to be two-dimensional histogram for each reconstruction category.

4. Model For $B^0 \to (\rho^0\pi^0\pi^0)_{\mathrm{NR}}$ And $B^0 \to (f_0\pi^0\pi^0)_{\mathrm{NR}}$ Decays

The modes $B \to (\rho^0\pi^0\pi^0)_{\mathrm{NR}}$ and $B \to (f_0\pi^0\pi^0)_{\mathrm{NR}}$ have almost identical distributions and are therefore combined to one component, referred to as $X^0\pi^0\pi^0$. These decays exhibit certain kinematic behaviors of the dipion masses (flat distribution) and the helicity angles. Because the π^0 momenta are usually higher then those of the charged daughters of the ρ^0 (f_0), the helicity angles peak at $\cos\theta_{\mathrm{H}} = +1$. This kinematic behavior also occurs in other combinatorial backgrounds, e.g. other B decays involving a ρ^0 meson. Therefore, we add a component to the $X^0\pi^0\pi^0$ model where the PDFs of dipion masses and helicity angles are taken from the $X^0\pi^0\pi^0$ model, while the PDFs for ΔE and M_{bc} are taken from a combinatorial background ($B\bar{B}$ model). We determine the fraction of the combinatorial description within the $X^0\pi^0\pi^0$ model, $f_{\mathrm{comb}}^{X^0\pi^0\pi^0}$, in the fit to data in order to avoid a misidentification of combinatorial background as $B \to X^0\pi^0\pi^0$ due to the strong discrimination power of the helicity angles in this case.

The PDF for the mass distribution is take to be the product of a sum of a second and third order Chebychev polynomial for each dipion mass and the helicity PDF is taken to be a two-dimensional histogram.

E. Full Model

The total likelihood for 216176 events in the fit region is

$$\mathcal{L} \equiv \prod_{l,s} \frac{e^{-\sum_j N_j^s \sum_{l,s} f_j^{l,s}}}{N_{l,s}!} \prod_{i=1}^{N_{l,s}} \sum_j N_j^s f_j^{l,s} \mathcal{P}_j^{l,s}(\Delta E^i, M_{\mathrm{bc}}^i, \mathcal{F}_{S/B}^i, M_+^i, M_-^i, H_+^i, H_-^i, \Delta t^i, q^i), \quad (9)$$

which runs over event i, component j, r-bin l and SVD configuration s. Instead of two free signal yields N_{Sig}^s for each detector configuration, the branching fractions for the four-pion final states ($j \in 1, ... 7$) are chosen as single free parameters $\mathcal{B}(B \to X)$ and incorporated into the fit as

$$N_j^s = \mathcal{B}(B^0 \to f)N_{B\bar{B}}^s \epsilon_j^s \eta, \quad (10)$$

where ϵ_j^s are the signal selection efficiencies, fixed to the values listed in Table II. Using independent control samples, we determine the efficiency correction factor $\eta = \eta^{\pm} \cdot \eta^0$ that accounts for differences between data and MC in the charged particle identification for the two charged pions, $\eta^{\pm} = 0.93 \pm 0.03$, and π^0 reconstruction for two π^0 mesons, $\eta^0 = 0.91\pm0.03$. The uncertainties on both corrections are included in the systematic uncertainties of our results (see Section VII).

TABLE IV: Summary of the fixed ratios of the yields of charmed and charmless B^+B^- background relative to the respective floated number of $B^0\bar{B}^0$ background events for the two detector configurations s. The central values are obtained from MC simulation; the errors are statistical.

Component	Yield SVD1	Yield SVD2
$N_{B^+B^-}^{\mathrm{charm},s}$	$(1.78 \pm 0.02)N_{B^0\bar{B}^0}^{\mathrm{charm,SVD1}}$	$(2.02 \pm 0.01)N_{B^0\bar{B}^0}^{\mathrm{charm,SVD2}}$
$N_{B^+B^-}^{\mathrm{charmless},s}$	$(1.04 \pm 0.02)N_{B^0\bar{B}^0}^{\mathrm{charmless,SVD1}}$	$(1.00 \pm 0.01)N_{B^0\bar{B}^0}^{\mathrm{charmless,SVD2}}$

TABLE V: List of peaking backgrounds, assumed branching fractions and their expected yields $N_{\mathrm{expected}}^{\mathrm{s}}$ for the two detector configurations; SVD1 and SVD2.

Mode	$\mathcal{B}$ $(\times 10^{-6})$	$N_{\mathrm{expected}}^{\mathrm{SVD1}}$	$N_{\mathrm{expected}}^{\mathrm{SVD2}}$
$B^0 \to a_1^{\pm}[\pi^{\pm}\pi^0\pi^0]\pi^{\mp}$	$0.5 \times (26 \pm 5)$	11	52
$B^0 \to \omega[\pi^+\pi^-\pi^{\pm}]\pi^0$	0.5 ± 0.5	0	1

Eq. (10) takes the distinct forms for the two possible polarization states of the ρ meson: for longitudinally polarized ρ mesons (LP),

$$N_{\mathrm{LP}}^s = \mathcal{B}(B^0 \to \rho^+\rho^-)f_L N_{B\bar{B}}^s \epsilon_{\mathrm{LP}}^s \eta_{\mathrm{LP}}^s, \tag{11}$$

and similarly for transversely polarized ρ mesons, with $(1 - f_L)$ replacing f_L. The fraction of events in each r-bin l for component j is denoted by $f_j^{l,s}$ and fixed according to MC simulation for all B decays.

In the fit to data, we float 94 parameters in total. Besides the branching fraction, f_L and the CP violating parameters $\mathcal{A}_{CP}$ and $\mathcal{S}_{CP}$ of the decay $B^0 \to \rho^+\rho^-$, the free parameters are the branching fractions of $B \to (\pi^+\pi^0\pi^-\pi^0)_{\mathrm{NR}}$, $(\rho^{\pm}\pi^{\mp}\pi^0)_{\mathrm{NR}}$, $a_1^0\pi^0$, $X^0\pi^0\pi^0$, as well as the yields $N_{q\bar{q}}^s$, $N_{B^0\bar{B}^0}^{\mathrm{charm},s}$ and $N_{B^0\bar{B}^0}^{\mathrm{charmless},s}$. The remaining free parameters describe the shape of the continuum model. The remaining yields are fixed to the values determined from MC simulation as given in Tables IV and V.

For ΔE, M_{bc} and $\mathcal{F}_{S/B}$, we incorporate calibration factors to correct for possible differences between the data and MC distributions. They are determined from a large-statistics control sample $B^+ \to \bar{D}^0[K^+\pi^-\pi^0]\rho^+$ and are used to calibrate the means and widths of the core bifurcated Gaussian functions for the ΔE and M_{bc} PDFs of all four-pion final states, and of the $\mathcal{F}_{S/B}$ PDFs of all $B\bar{B}$ components. Similarly, we correct the fractions of events in each r-bin for all $B\bar{B}$ components. Furthermore, the core Gaussian functions of the signal are contraint to be common for all four-charged-pion final states for ΔE and M_{bc} and for all $B\bar{B}$ modes for $\mathcal{F}_{S/B}$.

V. RESULTS

From the fit to the data, described in the previous section, we obtain

$$\mathcal{B}(B^0 \to \rho^+\rho^-) = (28.3 \pm 1.5 \text{ (stat)} \pm 1.5 \text{ (syst)}) \times 10^{-6},$$
$$f_L = 0.988 \pm 0.012 \text{ (stat)} \pm 0.023 \text{ (syst)},$$
$$\mathcal{A}_{CP} = 0.00 \pm 0.10 \text{ (stat)} \pm 0.06 \text{ (syst)},$$
$$\mathcal{S}_{CP} = -0.13 \pm 0.15 \text{ (stat)} \pm 0.05 \text{ (syst)}.$$

corresponding to 1754 ± 94 and 21 ± 22 $B^0 \to \rho^+\rho^-$ events with longitudinal and transverse polarization, respectively. The evaluation of the systematical uncertainties given above is described in Section VII. Signal-enhanced projections of the fit results onto ΔE, M_{bc}, M_+, M_-, H_+, H_- and $\mathcal{F}_{S/B}$ are shown in Fig. 4, where the signal-enhanced region is defined as $|\Delta E| < 0.1$ GeV, $M_{\text{bc}} > 5.275$ GeV/c^2, 0.62 GeV/$c^2 < m(\pi^\pm\pi^0) < 0.92$ GeV/c^2, $\mathcal{F}_{S/B} > 0.75$, and r-bin> 2. Depending on the projected variable 10% - 16% of the signal events are retained.

A clear signal peak can be seen in the ΔE and M_{bc} distributions, while the signal-enhanced projection onto $\mathcal{F}_{S/B}$ remains dominated by the continuum contribution. The $\rho^\pm$ mesons are found to be predominantly in the longitudinally polarized state. Figure 5 (a) shows the flavor-integrated Δt distribution, including the fit result. No CP violation is observed: the Δt distributions for the two flavors of B^0_{tag} in Fig. 5 (b) lacks any asymmetry. The statistical correlation coefficients between the observables are given in Table VI and are all negligible except for a correlation between $\mathcal{B}(B^0 \to \rho^+\rho^-)$ and f_L. The yields of all other four-pion final states are shown in Table VII and are consistent with zero within 90% confidence level except for the $X^0[\pi^+\pi^-]\pi^0\pi^0$ component, being consistent with combinatorial background. We do not provide the converted branching fractions of the peaking background modes as the systematic uncertainties are expected to be large for the four-pion backgrounds.

TABLE VI: Correlation matrix as obtained from the fit to the data.

	$\mathcal{B}(B^0 \to \rho^+\rho^-)$	f_L	$\mathcal{A}_{CP}$	$\mathcal{S}_{CP}$
$\mathcal{B}(B^0 \to \rho^+\rho^-)$	1	-0.228	-0.031	-0.015
f_L		1	0.003	0.026
$\mathcal{A}_{CP}$			1	0.018
$\mathcal{S}_{CP}$				1

VI. VALIDITY CHECKS

We have validated the fitting procedure by studying a large number of pseudo experiments, where either all components are generated from the PDFs or all $B\bar{B}$ components are taken from a full GEANT MC simulation. Within the statistical error, the fitter reliably recovers the input values for f_L and $\mathcal{S}_{CP}$. For the branching fraction and $\mathcal{A}_{CP}$, the fitter exhibits a small bias in the case of fully simulated events due to imperfections in the modeling of the variable correlations. The treatment of the bias is described in Section VII. The errors from the fit results are consistent with the expectations from studying fully simulated

TABLE VII: Yields of the four-pion final states as obtained from the fit to the data. The errors are statistical only. The component $X^0\pi^0\pi^0$ is treated as explained in the text, see Section IV D. The fraction $f_{\text{comb}}^{X^0\pi^0\pi^0}$ is consistent with one and excludes a significant contribution of $B^0 \to X^0[\pi^+\pi^-]\pi^0\pi^0$ decays.

Mode	Yield	$f_{\text{comb}}^{X^0\pi^0\pi^0}$
$B^0 \to a_1^0\pi^0$	86 ± 94	$--$
$B^0 \to (\rho^\pm\pi^\mp\pi^0)_{\text{NR}}$	215 ± 131	$--$
$B^0 \to (\pi^+\pi^0\pi^-\pi^0)_{\text{NR}}$	170 ± 114	$--$
$X^0\pi^0\pi^0$	625 ± 90	1.12 ± 0.16

MC events. We check the fitting procedure by floating the B^0 lifetime in a separate fit. The obtained lifetime is consistent with the current world average within one statistical standard deviation.

We furthermore perform three checks, where we either require $|r| > 0.5$ or $\mathcal{F}_{S/B} > 0.5$ or where we set the fractions of the signal's 1T and 0T components to zero in fits to the data. All results are consistent with our baseline result. We perform a fit to data, where we require $0.78 \text{ GeV}/c^2 < m(\pi^\pm\pi^0) < 0.86 \text{ GeV}/c^2$ to test the assumptions made in the isospin analysis [48]. This removes events with different ρ^+ and ρ^- masses, which breaks the isospin symmetry assumed in the determination of ϕ_2. We obtain $\mathcal{S}_{CP} = -0.09 \pm 0.21$ (stat), being consistent with our nominal result.

In order to determine the data-to-simulation correction factors (see Section IV), we study a control sample of $B^+ \to \bar{D}^0[K^+\pi^-\pi^0]\rho^+$ decays, which are topologically similar to $B^0 \to \rho^+\rho^-$. We perform fits including ΔE, M_{bc}, $\mathcal{F}_{S/B}$, $m(\pi^\pm\pi^0)$, $\cos\theta_{\text{H}}^\pm$ and Δt. The results obtained for the branching fraction, the fraction of longitudinal polarized $\rho^\pm$ mesons and also the $B^\pm$ lifetime are in agreement with the current world averages within one statistical standard deviation [39]. In addition, the time-dependent CP-violation parameters are consistent with zero when floating them in the fit to the data.

VII. SYSTEMATIC UNCERTAINTIES

Systematic uncertainties from various sources are considered and estimated with independent studies and cross checks and are summarized in Table VIII. For the total systematic uncertainties, the components are added in quadrature. They include the uncertainty on the number of produced $B\bar{B}$ events, the track-reconstruction efficiency, the selection efficiency due to particle identification, and the π^0 reconstruction, which are determined by using independent control samples. The π^0 efficiency correction is obtained from studying $\tau^\pm \to \pi^\pm\pi^0\nu_\tau$ decays. In the previous Belle measurement, this difference between data and MC was studied with $\eta \to \pi^0\pi^0$, $\pi^0\pi^0\pi^0$ decays and was fully treated as a systematic uncertainty. Uncertainties affecting the vertex reconstruction include the interaction point (IP) profile, the track selection based on the track helix errors, helix parameter corrections, the tag side track selection based on their impact parameters, Δt and vertex goodness-of-fit selection, Δz bias and SVD misalignment. The Δt resolution function parameters, as well as the flavor tagging performance parameters w and Δw, are varied within their errors. Possible systematic biases from the interference on the tag side arising between the CKM-favored

$b \rightarrow c\bar{u}d$ and doubly CKM-suppressed $\bar{b} \rightarrow \bar{u}c\bar{d}$ amplitudes in the final states used for flavor tagging are estimated by studying a large number of MC pseudo-experiments generated with interference [47]. The input parameters for the pseudo-experiments and the amount of their possible changes are estimated by the semileptonic B decay control sample, $B^0 \rightarrow D^{*-}l^+\nu$.

The parametric model shape is varied within the errors obtained from MC simulation. The fixed ratios listed in Table IV are varied within $\pm 10\%$ and give a negligible contribution. Uncertainties in the non-parametric shapes are obtained by varying the contents of the histogram bins within $\pm 1\sigma$ in turn. The fixed physics parameters, the $\rho^\pm$ mass and width as well as the τ_{B^0} and Δm, are varied within their world-average uncertainties [39]. To account for a possible difference in the distributions obtained from MC simulation to data, we vary the fractions of the combinatorial part (reconstruction category $0T$) by $\pm 20\%$ for all components including a ρ resonance in turn.

We account for a difference between data and MC by varying the fraction of the different signal categories by $\pm 20\%$ of their values and repeating the fit. The systematic uncertainty due to fixing the peaking background yield $B \rightarrow \omega\pi^0$ is estimated by varying the branching fraction by its world average error and repeating the fit. For $B^0 \rightarrow a_1^\pm\pi^\mp$ we vary the yield by a conservative factor of two while also increasing the fraction of correctly reconstructed events. This is motivated by the high sensitivity of the reconstruction efficiency of this decay to the dipion analysis region and a possible difference in the line shape between MC simulation and data.

The fit bias is determined from full simulation by examining the difference between the generated and fitted physics parameters. Because of imperfections in the modeling of the correlations, we find a non-negligible but stable bias of $+0.5 \times 10^{-6}$ for the branching fraction of $B^0 \rightarrow \rho^+\rho^-$ and of $+0.04$ for $\mathcal{A}_{CP}$. We study these biases with large statistics ensemble tests, and correct the result. The systematic uncertainties related to the bias correction are obtained from studying pseudo experiments generated with the observables varied within ± 1 statistical standard deviation of the fit result. The largest deviations to the generated values is then taken. All other biases are found to be small compared to the statistical uncertainty and are therefore treated fully as systematic uncertainties.

The dominant uncertainty of the CP-violating parameters is due to a possible CP violation in the $B\bar{B}$ backgrounds. We include an asymmetry term in the Δt PDFs of the $B\bar{B}$ backgrounds and refit the data, where the asymmetry is fixed to $\pm 5\%$ CP violation for charm B decays and $\pm 50\%$ for charmless B decays in turn. Only direct CP violation is considered for charged B decays and we provide the uncertainties from the four-pion final state backgrounds and from the remaining $B\bar{B}$ decays separately in Table VIII.

We account for the phase space assumption for $B^0 \rightarrow (\rho^\pm\pi^\mp\pi^0)_{\mathrm{NR}}$ decays by replacing the helicity PDF with one where the two non-resonant pions are either in a S- or a P-wave configuration in the fit to the data. In the latter case, the $\rho^\pm$ can be either longitudinally or transversely polarized. The maximal deviation from the nominal model is taken as the uncertainty related to the assumption of the $B^0 \rightarrow (\rho^\pm\pi^\mp\pi^0)_{\mathrm{NR}}$ helicity dependence. This is the dominant uncertainty in the measurement of f_L.

Finally, the uncertainty from neglecting interference between the four-pion final states is estimated by constructing a 4-body amplitude model and studying samples of two four-pion final states, including detector effects. For each set of modes, we first calibrate the relative amplitude strength between two considered modes in order to obtain a yield ratio as found in the data. For the calibration, we set the relative phase to $90°$. Then we generate sets where the relative phase between the two modes of interest varies from $0°$ to $180°$ in steps of

$10°$. Each set is fitted with an incoherent model and the largest root-mean-square error of the variation of the fit results is taken to be the systematic uncertainty for each observable. We consider the modes $B^0 \to \rho^+\rho^-, a_1^\pm\pi^\mp, (\rho^\pm\pi^\mp\pi^0)_{\mathrm{NR}}$, and $(\pi^+\pi^0\pi^-\pi^0)_{\mathrm{NR}}$, and find that interference is almost negligible.

Due to the large variety of backgrounds, changes in the model tend to affect the background yields, while leaving the signal yield rather stable.

(a)

Arbitrary Units L_2^c(GeV/c)

Arbitrary Units L_0^n(GeV/c)

Arbitrary Units L_2^n(GeV/c)

Arbitrary Units $|cos(TB,TO)|$

Arbitrary Units $|cos(TB,z)|$

Arbitrary Units $cos(B,z)$

Arbitrary Units h_{so}^{02}(GeV^2/c^2)

Arbitrary Units h_{so}^{04}(GeV^2/c^2)

Arbitrary Units h_{so}^{10}(GeV^2/c^2)

Arbitrary Units h_{so}^{12}(GeV^2/c^2)

Arbitrary Units h_{so}^{14}(GeV^2/c^2)

Arbitrary Units h_{oo}^{2}(GeV^2/c^2)

(b)

normalized # events/ (0.07)

$F_{S/B}$
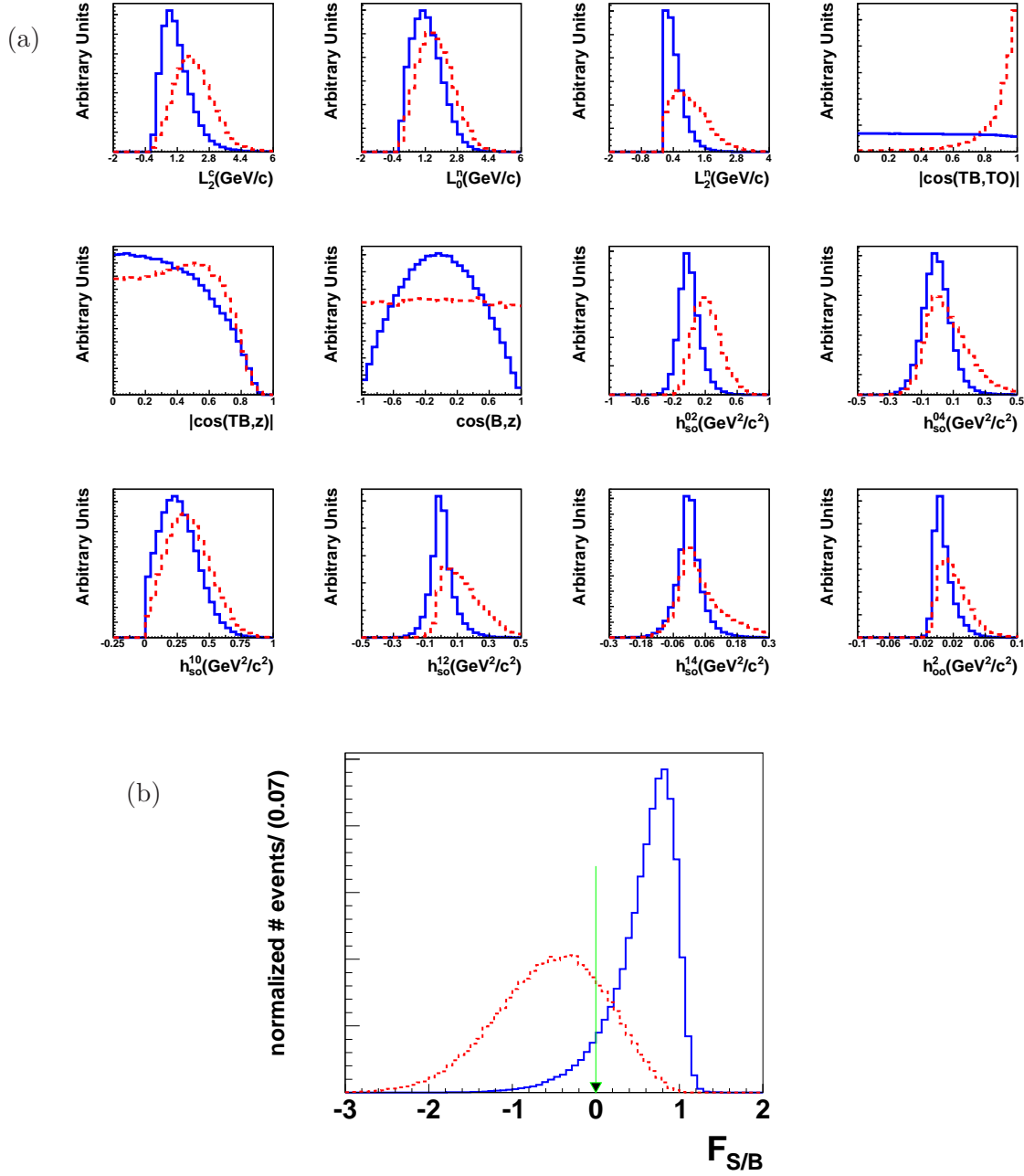
FIG. 3: (color online) (a) Simulated MC and off-resonance data distributions for the quantities used to construct the Fisher discriminant $\mathcal{F}_{S/B}$. The solid (blue) histograms show the distribution for $B\bar{B}$ MC events, while the dashed (red) histograms show the distributions for events from off-resonance data, both normalized to the same area.

(b) Output of the fisher discriminant. The same line (color) scheme is used as above. The green arrow indicates the requirement of $\mathcal{F}_{S/B} > 0$.

23
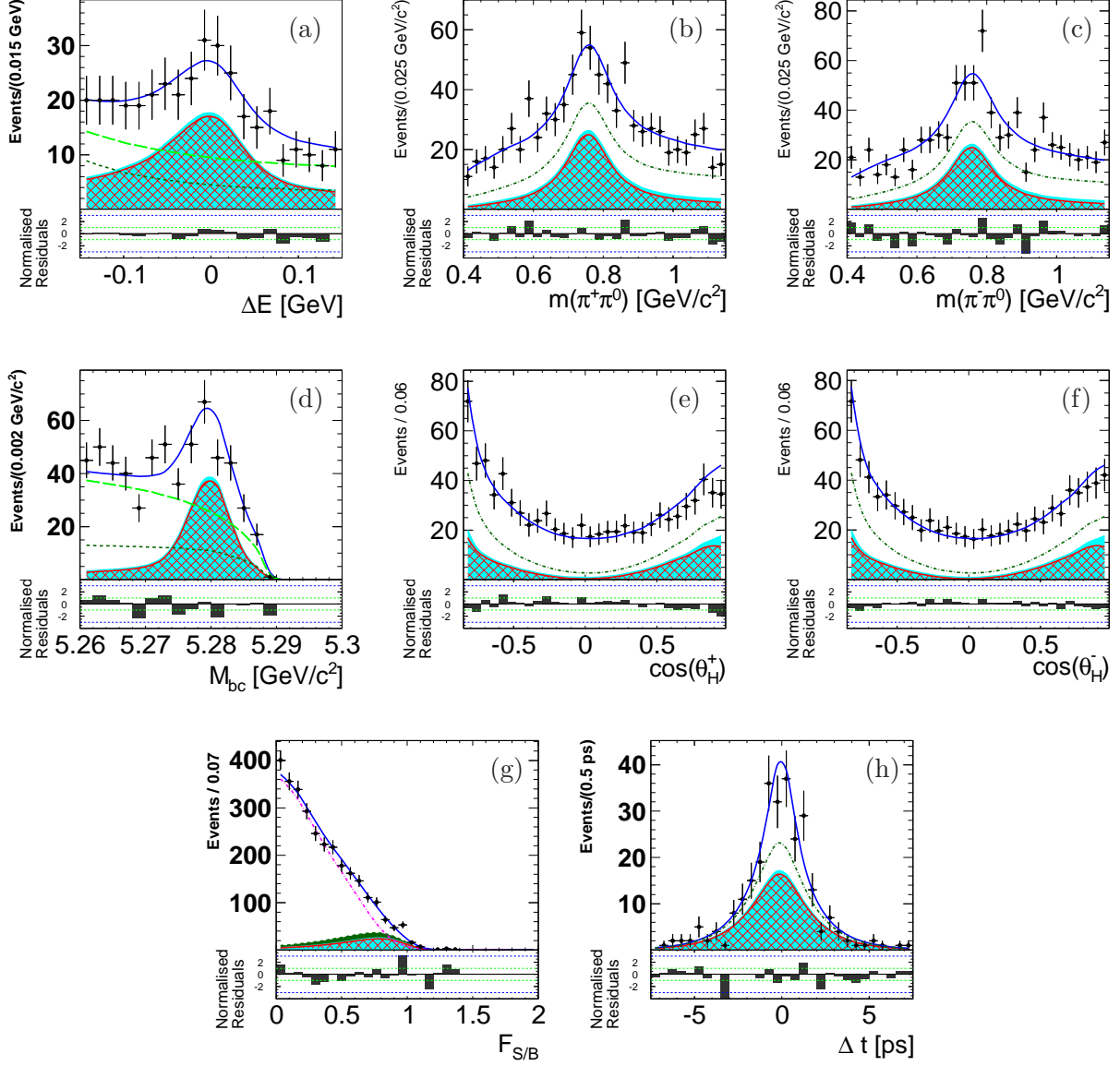
FIG. 4: (color online) Projections of the fit to the data in signal-enhanced regions as described in the text. The (black) points represent the data and the solid (blue) curves represent the fit result. The hashed (red) areas show the $B^0 \to \rho^+\rho^-$ contribution and the bright-shaded (cyan) areas show all four-pion final states. (a) and (d): the short-dashed (dark green) curves show the non-peaking $B\bar{B}$ contribution and the long-dash (bright green) curves show the total non-peaking background. (b), (c), (e) and (f): the dash-dotted (dark green) line shows the contribution from all $B\bar{B}$ decays. (g): the dash-dotted (magenta) curve shows the continuum contribution, the dark (green) area shows the entire contribution from $B\bar{B}$ decay. (h): the dashed (dark green) curve shows the non-peaking $B\bar{B}$ contribution. The residuals are plotted below each distribution.
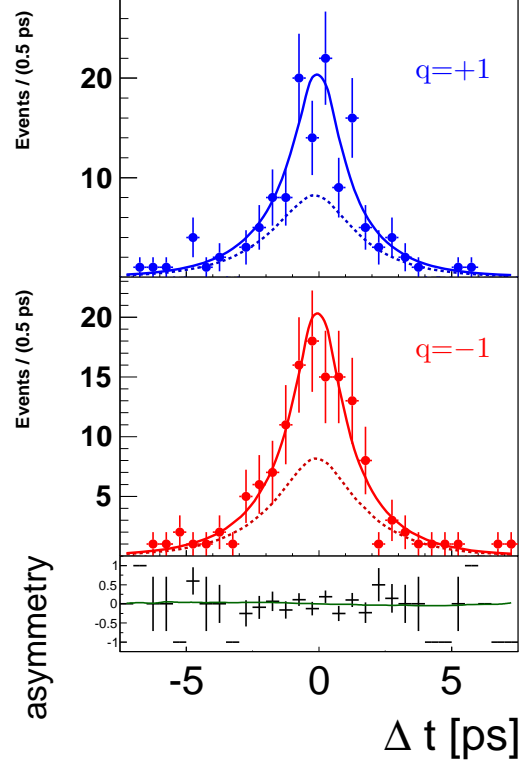
FIG. 5: (color online) Projections of the fit result onto Δt for each flavor of B^0_{tag}. The points represent the data and the solid curves represent the fit result. Signal is shown as a dashed line. The measured asymmetry is plotted below.

TABLE VIII: Systematic uncertainties.

Category	$\delta\mathcal{B}(\%)$	δf_L	$\delta\mathcal{A}_{CP}[10^{-2}]$	$\delta\mathcal{S}_{CP}[10^{-2}]$
$N(B\bar{B})$	1.38	-	-	-
Tracking	0.70	-	-	-
PID	2.50	-	-	-
π^0 reconstruction	2.98	-	-	-
IP profile	0.01	0.001	0.68	0.94
Δt selection	0.00	0.001	0.04	0.06
Track helix error	0.00	0.000	0.02	0.01
Vertex quality	0.16	0.000	1.20	0.60
Tagside track selection	0.01	0.001	0.84	0.95
Δz bias	-	-	0.50	0.40
Misalignement	-	-	0.40	0.20
Resolution function	0.00	0.000	0.00	0.00
Flavor tagging	0.07	0.002	0.71	0.51
Tagside interference	-	-	1.02	0.08
Model shape	3.47	0.003	0.30	0.60
Histogram shape	0.17	0.002	0.19	0.31
Physics parameters	0.00	0.000	0.02	0.02
MC composition	0.04	0.007	0.64	1.34
Misreconstructed fraction	0.01	0.001	0.60	0.50
Fixed background yields	0.00	0.001	0.04	0.08
$B \to a_1^{\pm}\pi^{\mp}$ description	0.01	0.002	0.09	0.20
Fit bias	0.53	0.002	0.50	0.74
Background CP violation	0.00	0.000	4.92	2.75
$B \to 4\pi$ CP violation	0.03	0.006	3.03	3.65
$(\rho^{\pm}\pi^{\mp}\pi^0)_{\mathrm{NR}}$ helicity	0.04	0.020	0.12	0.77
Interference	0.01	0.002	0.12	0.15
Total	5.47	0.023	6.37	5.42
(absolute uncertainty $[\times 10^6]$)	1.55			

VIII. CONSTRAINTS ON THE CKM ANGLE ϕ_2

As stated in the Introduction, the CP violating parameters of the decay $B^0 \rightarrow \rho^+ \rho^-$ obtained in this paper can be used to constrain the angle ϕ_2 in the CKM unitarity triangle. In the following, we estimate the possible pollution from loop diagrams with two methods: isospin invariance and SU(3) flavor symmetry.

A. Isospin

We use our result together with other Belle results to obtain a constraint on ϕ_2 from a isospin analysis [24] in the $B \rightarrow \rho\rho$ system. Neglecting electroweak contributions or isospin-breaking effects, the complex $B \rightarrow \rho\rho$ amplitudes for the various charge configurations of the $\rho\rho$ system can be related via

$$\frac{1}{\sqrt{2}} A_{+-} + A_{00} = A_{+0}, \qquad \frac{1}{\sqrt{2}} \bar{A}_{+-} + \bar{A}_{00} = \bar{A}_{-0}, \tag{12}$$

where the amplitudes with $\bar{b} \rightarrow \bar{u}$ ($b \rightarrow u$) transitions are denoted as A_{ij} ($\bar{A}_{ij}$) and the subscripts identify the charges of the two ρ mesons. These relations can be visualized as two isospin triangles, as shown in Fig. 6. Since the charged B decay $B^\pm \rightarrow \rho^\pm \rho^0$ proceeds
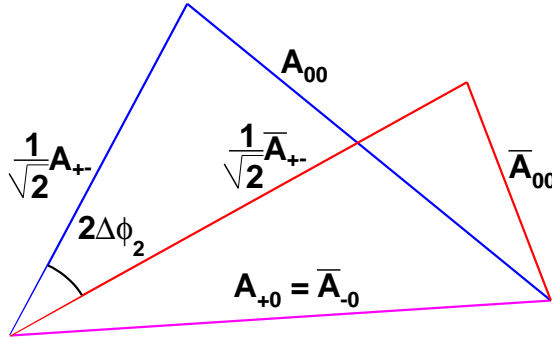
FIG. 6: Sketch of the isospin triangles for B and $\bar{B}$ decays into unflavored final states with isospin I=1.

only via a tree level diagram, the two isospin triangles share the same base $A_{+0} = \bar{A}_{-0}$. The phase difference between the two sides A_{+-} and $\bar{A}_{+-}$ corresponds to the shift $2\Delta\phi_2$ due to additional contributions. This method leads to an eight-fold ambiguity in the determination of ϕ_2, as there are four possible orientations of the two triangles and two solutions from the trigonometric conversion of $\sin(\phi_2^{\text{eff}})$. The amplitudes are constructed from the branching fractions and the direct CP asymmetries $\mathcal{A}_{CP}$ and are then used to obtain the possible pollution in the mixing-induced CP asymmetry $\mathcal{S}_{CP} = \sqrt{1 - A_{CP}^2} \sin(2\phi_2^{\text{eff}})$, obtained from the measurement of $B^0 \rightarrow \rho^+ \rho^-$ decays. The remaining sides of the triangles are constructed from other Belle results: the longitudinally polarized fraction of $\mathcal{B}(B^0 \rightarrow \rho^0 \rho^0) = (1.02 \pm 0.34) \times 10^{-6}$ with $f_L^{00} = 0.21 \pm 0.25$ [19] and the longitudinally polarized fraction of $\mathcal{B}(B^\pm \rightarrow \rho^\pm \rho^0) = (31.7 \pm 8.8) \times 10^{-5}$ with $f_L^{+0} = 0.95 \pm 0.11$ [49]. We convert the χ^2 distribution constructed from the five amplitudes, including the correlations obtained from this measurement, into a probability scan as shown in Fig. 7 (a).

Two solutions for ϕ_2 are found, the one that is consistent with other SM-based constraints yields $\phi_2 = (93.7 \pm 10.6)°$. The size of the penguin contributions is consistent with zero: $\Delta\phi_2 = (0.0 \pm 9.6)°$. Because of the very small $B^0 \to \rho^0\rho^0$ branching fraction relative to the other two $B \to \rho\rho$ decays, the four solutions from the isospin analysis collapse into the two distinct solutions.
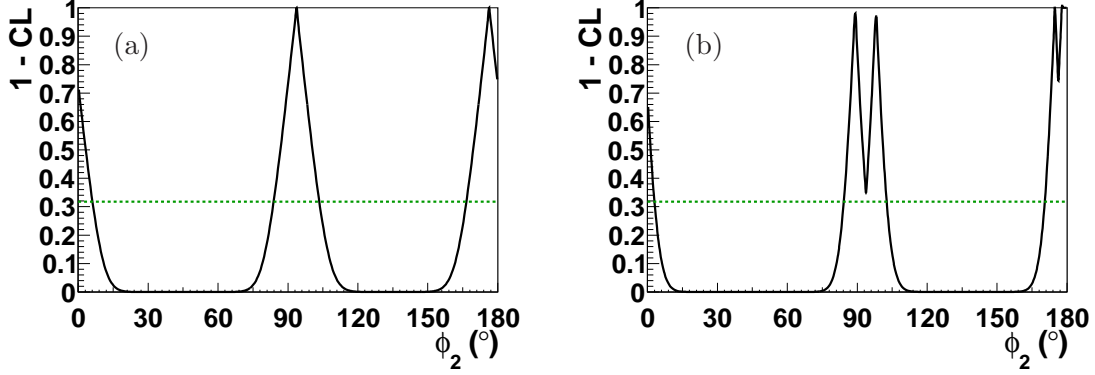

FIG. 7: $1-$CL versus ϕ_2 obtained from $B \to \rho\rho$ decays. (a) isospin analysis, (b) SU(3) flavor analysis. The horizontal line shows the 68% CL.

B. SU(3) Flavor

The amplitude of $B^0 \to \rho^+\rho^-$ decays can be written in terms of tree and penguin contributions

$$\mathcal{A}_{B^0 \to \rho^+\rho^-} = Te^{i\phi_3} + Pe^{i\delta_{PT}}, \tag{13}$$

where T and P are the magnitude of the tree and penguin amplitudes, respectively, δ_{PT} is their strong-phase difference and ϕ_3 is the phase of V_{ub}. Following Ref. [25], the SU(3) symmetry provides an alternative way to remove the penguin contribution from ϕ_2^{eff} by relating $B^0 \to \rho^+\rho^-$ decays to the pure penguin mode $B^+ \to K^{0*}\rho^+$:

$$\frac{\mathcal{B}_{\text{LP}}(B^+ \to K^{*0}\rho^+)}{\mathcal{B}_{\text{LP}}(B^0 \to \rho^+\rho^-)} = \frac{\tau_{B^\pm}}{\tau_{B^0}} \left(\frac{|V_{cs}|f_{K^*}}{|V_{cd}|f_\rho} \right)^2 \frac{Fr_{PT}^2}{1 - 2r_{PT}\cos\delta_{PT}\cos(\phi_1 + \phi_2) + r_{PT}^2}, \tag{14}$$

where $r_{PT} = |P|/|T|$ and the factor $F = 0.9 \pm 0.6$ is taken from Ref. [25] and accounts for possible SU(3) breaking ($F = 1$ corresponds to no breaking). $\mathcal{B}_{\text{LP}}$ denotes the branching fractions for longitudinal polarization; $\tau_{B^\pm}$ and τ_{B^0} the $B^\pm$ and B^0 lifetimes, respectively; V_{ij} is a CKM matrix element; and f_k is a form factor. The CKM phase ϕ_1 is taken from the measurement of $b \to c\bar{c}s$ decays [4] and $B^+ \to K^{0*}\rho^+$ related inputs from [50]. With

$$-\mathcal{A}_{CP} = \frac{2r_{PT}\sin\delta_{PT}\sin(\phi_1 + \phi_2)}{1 - 2r_{PT}\cos\delta_{PT}\cos(\phi_1 + \phi_2) + r_{PT}^2} \tag{15}$$

$$\mathcal{S}_{CP} = \frac{\sin 2\phi_2 + 2r_{PT}\cos\delta_{PT}\sin(\phi_1 - \phi_2) - r_{PT}^2\sin 2\phi_1}{1 - 2r_{PT}\cos\delta_{PT}\cos(\phi_1 + \phi_2) + r_{PT}^2}, \tag{16}$$

a probability scan similar to the isospin analysis can be performed, as shown in Fig. 7 (b), where each of the two double peaks consists of one solution for $\delta_{PT} < 90°$ and one otherwise.

The solution most compatible with other SM-based constraints and for the theoretically motivated case $\delta_{PT} < 90°$ is $\phi_2 = (89.3 \pm 4.8 \text{ (scan)}^{+1.0}_{-3.4} \text{ (SU(3))})°$. Varying F within the quoted error results in the second uncertainty, denoted as "SU(3)". We furthermore obtain $r_{PT} = 0.09 \pm 0.02 \text{ (scan)}^{+0.06}_{-0.02} \text{ (SU(3))}$ and $\delta_{PT} = (0.0 \pm 48.7 \text{ (scan)} \pm 0.0 \text{ (SU(3))})°$.

IX. CONCLUSIONS

We have presented measurements of the branching fraction of $B^0 \to \rho^+\rho^-$ decays, the fraction of longitudinally polarized $\rho^\pm$ mesons, as well as the CP-violating parameters in the decay into a pair of longitudinally polarized ρ mesons using the final Belle data set of 772×10^6 $B\bar{B}$ pairs. Improvements compared to previous Belle measurements are the increased data sample and the simultaneous extraction of all observables. The measurement is optimized for a high signal yield, as the CP-violating parameters are still statistically limited. The inclusion of the helicity angles provides additional and strong separation power between the various components and the simultaneous fit to Δt improves the continuum separation in particular. This procedure reduces the statistical uncertainties significantly at the cost of higher analysis complexity and a longer computing time. The obtained results are in excellent agreement with the previous measurements [16–18] and predictions [31, 33] and are currently the most precise measurement of the branching fraction and longitudinal polarization fraction as well as the tightest constraint on CP violation in this decay. We use our results, together with other Belle measurements of $B \to \rho\rho$ decays, to constrain the internal angle ϕ_2 of the CKM unitarity triangle with an isospin analysis. We obtain $\phi_2 = (93.7 \pm 10.6)°$ as the solution most compatible with other SM-based fits. The uncertainty of this scan is dominated by the large uncertainty on the branching fraction for the decay $B^\pm \to \rho^\pm\rho^0$. We provide an alternative constraint on ϕ_2 by exploiting the SU(3) flavor symmetry and obtain $\phi_2 = (89.3 \pm 4.8 \text{ (scan)}^{+1.0}_{-3.4} \text{ (SU(3))})°$ for the theoretically motivated case of $\delta_{PT} < 90°$.

[1] N. Cabibbo, Phys. Rev. Lett. **10**, 531 (1963).

[2] M. Kobayashi and T. Maskawa, Prog. Theor. Phys. **49**, 652 (1973).

[3] K. Abe *et al.* (Belle Collaboration), Phys. Rev. Lett. **87**, 091802 (2001).

[4] I. Adachi *et al.* (Belle Collaboration), Phys. Rev. Lett. **108**, 171802 (2012).

[5] B. Aubert *et al.* (BaBar Collaboration), Phys. Rev. Lett. **87**, 091801 (2001).

[6] B. Aubert *et al.* (BaBar Collaboration), Phys. Rev. D **79**, 072009 (2009).

[7] Here and in the following the charge-conjugated transition is implied unless otherwise stated.

[8] J. Brodzicka *et al.*, Prog. Theor. Exp. Phys. **2012**, 04D001 (2012).

[9] M. Battaglia, A. J. Buras, P. Gambino, A. Stocchi, *et al.*, arXiv:hep-ph/0304132.

[10] J. Charles *et al.* (CKMfitter Group), Eur. Phys. J. C41, 1-131 (2005) [hep-ph/0406184], updated results and plots available at: http://ckmfitter.in2p3.fr .

[11] H. Ishino *et al.* (Belle Collaboration), Phys. Rev. Lett. **98**, 211801 (2007).

[12] B. Aubert *et al.* (BaBar Collaboration), Phys. Rev. D **87**, 052009 (2013).

[13] R. Aaij *et al.* (LHCb Collaboration), JHEP **1210**, 037 (2012).

[14] A. Kusaka *et al.* (Belle Collaboration), Phys. Rev. Lett. **98**, 221602 (2007).

[15] B. Aubert *et al.* (BaBar Collaboration), Phys. Rev. D **76**, 012004 (2007).

[16] A. Somov *et al.* (Belle Collaboration), Phys. Rev. Lett. **96**, 171801 (2006).

[17] A. Somov *et al.* (Belle Collaboration), Phys. Rev. D **76**, 011104 (2007).

[18] B. Aubert *et al.* (BaBar Collaboration), Phys. Rev. D **76**, 052007 (2007).

[19] P.Vanhoefer *et al.* (Belle Collaboration), Phys. Rev. D **89**, 072008 (2014).

[20] B. Aubert *et al.* (BaBar Collaboration), Phys. Rev. D **78**, 071104 (2008).

[21] J. Dalseno *et al.* (Belle Collaboration), Phys. Rev. D **86**, 092012 (2012).

[22] B. Aubert *et al.* (BaBar Collaboration), Phys. Rev. Lett. **97**, 051802 (2006).

[23] B. Aubert *et al.* (BaBar Collaboration), Phys. Rev. Lett. **98**, 181803 (2007).

[24] M. Gronau and D. London, Phys. Rev. Lett. **65**, 3381 (1990).

[25] M. Beneke, M.Gronau, S. Jaeger and M. Spranger, Phys. Lett. B **638**, 68 (2006).

[26] H. N. Li and S. Mishima, Phys. Rev. D **73**, 114014 (2006).

[27] W. Zou and Z. Xiao, Phys. Rev. D **72**, 094026 (2005).

[28] M. Beneke, G. Buchalla, M. Neubert, C. T. Sachrajda, Nucl. Phys. B **591**, 313 (2000).

[29] G. Buchalla, Heavy Quark Theory, CERN-TH/2002-018, arXiv:hep-ph/0202092.

[30] M. Bartsch, G. Buchalla, C. Kraus, arXiv:0810.0249v1.

[31] M. Beneke, J. Rohrer and D. Yang, Nucl. Phys. B **774**, 64 (2007).

[32] H.Y. Cheng, K.C. Yang, Phys. Rev. D **78**, 094001 (2008).

[33] G.Bell, V.Pilipp, Phys. Rev. D **80**, 054024 (2009).

[34] S. Kurokawa and E. Kikutani, Nucl. Instr. and Meth. Phys. Res. Sect. A **499**, 1 (2003), and other papers included in this Volume; T.Abe *et al.*, Prog. Theor. Exp. Phys. **2013**, 03A001 (2013) and following articles up to 03A011.

[35] A. Abashian *et al.* (Belle Collaboration), Nucl. Instr. and Meth. Phys. Res. Sect. A **479**, 117 (2002), also see detector section in J.Brodzicka *et al.*, Prog. Theor. Exp. Phys. **2012**, 04D001 (2012).

[36] Z. Natkaniec *et al.* (Belle SVD2 Group), Nucl. Instr. and Meth.. A **560**, 1 (2006).

[37] R. Brun *et al.*, GEANT 3.21, CERN DD/EE/84-1 (1984).

[38] H. Tajima *et al.*, Nucl. Instr. and Meth. A **533**, 370 (2004).

[39] K.A. Olive *et al.* (Particle Data Group), Chin. Phys. C **38**, 090001 (2014).

[40] R. A. Fisher, Annals of Human Genetics **7**, 179 (1936).

[41] G.C. Fox and S. Wolfram, Phys. Rev. Lett. **41**, 1581 (1978).

[42] K. Abe *et al.* (Belle Collaboration), Phys. Lett. B **511**, 151 (2001).

[43] H. Kakuno *et al.* (Belle Collaboration), Nucl. Instrum. and Meth. A **533**, 516 (2004).

[44] P. Vanhoefer, Study of $B^0 \to \rho\rho$ decays with the Belle experiment. Dissertation, LMU München: Faculty of Physics, urn:nbn:de:bvb:19-183537 (2015).

[45] J. M. Blatt and V. F. Weisskopf, Theoretical Nuclear Physics (Wiley, New York, 1952).

[46] H. Albrecht *et al.* (ARGUS Collaboration), Phys. Lett. B **241**, 278 (1990).

[47] O. Long, M. Baak, R.N. Cahn, D. Kirkby, Phys. Rev. D **68**, 034010 (2003).

[48] A. F. Falk, Z. Ligeti, Y. Nir, and H. Quinn, Phys. Rev. D **69**, 011502(R) (2004).

[49] J. Zhang *et al.* (Belle Collaboration), Phys. Rev. Lett. **91**, 221801 (2003).

[50] J. Zhang *et al* (Belle Collaboration), Phys. Rev. Lett. **95**, 141801 (2005).

Appendix

A.   Signal Correlation Matrices

0	ΔE	M_{bc}	$m^1_{\pi^+\pi^-}$	$m^2_{\pi^+\pi^-}$	$\mathcal{F}_{S/B}$	$\cos\theta^1_{\mathrm{H}}$	$\cos\theta^2_{\mathrm{H}}$	Δt
ΔE	1	-0.01	0.04	0.04	0.00	-0.09	-0.09	0.00
M_{bc}		1	-0.00	-0.00	0.00	-0.02	-0.02	0.00
$m^1_{\pi^+\pi^-}$			1	-0.00	-0.03	-0.02	-0.00	0.00
$m^2_{\pi^+\pi^-}$				1	-0.02	0.00	-0.02	-0.00
$\mathcal{F}_{S/B}$					1	0.00	0.01	-0.00
$\cos\theta^1_{\mathrm{H}}$						1	-0.04	-0.00
$\cos\theta^2_{\mathrm{H}}$							1	0.00
Δt								1

TABLE IX: Correlation matrix for the truth model (LP, SVD2).

0	ΔE	M_{bc}	$m^1_{\pi^+\pi^-}$	$m^2_{\pi^+\pi^-}$	$\mathcal{F}_{S/B}$	$\cos\theta^1_{\mathrm{H}}$	$\cos\theta^2_{\mathrm{H}}$	Δt
ΔE	1	0.00	0.06	0.06	0.05	-0.03	-0.04	0.00
M_{bc}		1	-0.03	-0.02	0.03	0.03	0.02	0.00
$m^1_{\pi^+\pi^-}$			1	-0.02	-0.01	-0.11	0.08	0.00
$m^2_{\pi^+\pi^-}$				1	-0.02	0.08	-0.12	-0.01
$\mathcal{F}_{S/B}$					1	0.02	0.02	0.00
$\cos\theta^1_{\mathrm{H}}$						1	-0.40	0.00
$\cos\theta^2_{\mathrm{H}}$							1	-0.00
Δt								1

TABLE X: Correlation matrix for the 2T signal model (LP, SVD2).

0	ΔE	M_{bc}	$m^1_{\pi^+\pi^-}$	$m^2_{\pi^+\pi^-}$	$\mathcal{F}_{S/B}$	$\cos\theta^1_{\mathrm{H}}$	$\cos\theta^2_{\mathrm{H}}$	Δt
ΔE	1	0.01	0.01	0.02	0.04	-0.09	-0.09	-0.00
M_{bc}		1	-0.02	-0.02	0.03	0.02	0.03	-0.01
$m^1_{\pi^+\pi^-}$			1	-0.01	-0.00	0.04	-0.08	0.00
$m^2_{\pi^+\pi^-}$				1	-0.01	-0.08	0.06	0.00
$\mathcal{F}_{S/B}$					1	0.04	0.03	0.01
$\cos\theta^1_{\mathrm{H}}$						1	-0.39	0.01
$\cos\theta^2_{\mathrm{H}}$							1	0.01
Δt								1

TABLE XI: Correlation matrix for the signal 1T model (LP, SVD2).

0	ΔE	M_{bc}	$m^1_{\pi^+\pi^-}$	$m^2_{\pi^+\pi^-}$	$\mathcal{F}_{S/B}$	$\cos\theta^1_{\mathrm{H}}$	$\cos\theta^2_{\mathrm{H}}$	Δt
ΔE	1	-0.01	0.00	0.03	0.06	-0.05	-0.04	-0.02
M_{bc}		1	0.00	-0.02	0.03	0.05	0.05	0.01
$m^1_{\pi^+\pi^-}$			1	0.05	0.01	0.01	-0.00	-0.01
$m^2_{\pi^+\pi^-}$				1	-0.00	0.01	-0.01	0.01
$\mathcal{F}_{S/B}$					1	0.09	0.10	-0.00
$\cos\theta^1_{\mathrm{H}}$						1	-0.01	0.00
$\cos\theta^2_{\mathrm{H}}$							1	-0.01
Δt								1

TABLE XII: Correlation matrix for the signal 0T model (LP, SVD2).